Platform and Environmental Effects on Above- and In-Water Determinations of Water-Leaving Radiances

Stanford B. Hooker
NASA Goddard Space Flight Center
Greenbelt, Maryland

André Morel
Universit/'e Pierre et Marie Curie/CNRS
06238 Villefranche-sur-Mer, France

March 19, 2001 Submitted to Applied Optics

Abstract

A comparison of above- and in-water spectral measurements in Case-1 conditions showed the uncertainty in above-water determinations of water-leaving radiances depended on the pointing angle of the above-water instruments with respect to the side of the ship. Two above-water methods were used to create a diagnostic variable to quantify the presence of superstructure reflections which degraded the above-water intracomparisons of water-leaving radiances by 10.9–33.4% (for far-to-near viewing distances, respectively). The primary conclusions of the above- and in-water intercomparison of water-leaving radiances were as follows: a) the SeaWiFS 5% radiometric objective was achieved with the above-water approach, but reliably with only one method and only for about half the data; b) a decrease in water-leaving radiance values was seen in the presence of swell, although, wave crests were radiometrically brighter than the troughs; and c) standard band ratios used in ocean color algorithms remained severely affected, because of the relatively low signal and, thus, proportionally significant contamination at the 555 nm wavelength.

1. Introduction

Ocean color satellite sensors[1] provide large-scale synoptic observations of biogeochemical properties of the upper layer in the open ocean (e.g., phytoplankton biomass), as well as continuous monitoring of other important parameters in the coastal zones (e.g., sediment load and dissolved colored matter). This global capability is accomplished through the determination of radiometric quantities, specifically the spectral values of the radiances at the top of the atmosphere, from which (after atmospheric correction), the radiances emerging from the ocean surface, $L_W(\lambda)$, are extracted (λ denotes the wavelength).

For meaningful applications, an extremely high radiometric accuracy is required. For example, the Sea-viewing Wide Field-of-view Sensor (SeaWiFS) Project requires accuracies of 5% absolute and 1% relative in terms of the retrieved $L_W(\lambda)$ values.[2] The first obvious condition for reaching such an accuracy lies in the conception and the realization of the spaceborne instrument. Although this is a necessary requirement, it is not sufficient to ensure the distributed radiometric data meet the accuracy objectives. Indeed, the success of the SeaWiFS mission is determined in particular by the quality of the ocean color data set collected for calibration and validation purposes, and involves several continuous activities:[3] a) characterizing and calibrating the sensor system, b) analyzing trends and anomalies in the sensor performance and derived products (the L_W values and the chlorophyll concentration), c) supporting the development and validation of algorithms (for the retrieval of bio-optical properties and for atmospheric correction), and d) verifying the processing code and selecting ancillary data (e.g., ozone, wind, atmospheric pressure) used in the data processing scheme.

The initial SeaWiFS validation results[4] have provided an immediate and quantitative demonstration of the strengths of the initial calibration and validation plan:[5] a) the sensor has been stable over the first two years of operation, with gradual changes in some wavelengths being accurately quantified using the solar and lunar calibration data, b) the vicarious calibration approach using field data produces consistent $L_W(\lambda)$ values, and c) the remotely-sensed products, including the chlorophyll concentration, meet the desired accuracy (35% over a range 0.05–$50\,\mathrm{mg\,m^{-3}}$) over a limited, albeit diverse, set of open ocean validation sites.

This paper does not deal with all aspects of the calibration and validation process. It is restricted to those field measurements suitable for vicarious calibration, as well as the derivation or improvement of bio-optical algorithms. Historically, the fundamental radiometric quantities selected for comparison with the radiances measured by—or, more precisely, retrieved from—the spaceborne sensor, were the upwelled spectral radiances just above the sea surface, $L_W(\lambda, 0^+)$ (the symbol 0^+ means immediately above the surface). Various normalizations of these radiances (see below) are needed to render these quantities less dependent on the circumstances (in particular, on the solar illumination conditions prevailing when the measurements are performed), and thus, to obtain more fundamental quantities to be introduced into the bio-optical algorithms.

The $L_W(\lambda, 0^+)$ radiances can be derived by extrapolating in-water measurements taken close to the sea surface or obtained directly from above-water measurements. In-water techniques has been largely successful in Case-1 waters, but the above-water approach for vicarious calibration remains nevertheless attractive, because a) the data can presumably be collected more rapidly and from a ship underway, and b) the frequently turbid and strongly absorbing waters in shallow Case-2 environments impose severe limitations on in-water measurements, particularly because of the instrument self-shading effect. For both methods, protocols have been recommended[6] and revised.[7,8]

From a measurement point of view, the above-water problem is more restrictive, because there presently is no reliable mechanism for floating an above-water system away from a ship (which can be easily and effectively accomplished for an in-water system), so all above-water measurements are made in close proximity to the vessel. The objective of the present study, based on a high quality data set collected during a one-month field campaign in Case-1 waters and under excellent sky and sea-state conditions, is to compare both techniques in various geometrical conditions (pointing angle plus sun and ship positions), and to examine several problems associated with above-water determinations, particularly those caused by the perturbations due to the ship itself and also to other environmental factors, such as oceanic swell.

2. Theoretical Framework

The basic equations relating the upward radiance field below the surface with that exiting the surface, the angular bidirectional dependency of these fields, and the transformation of radiance or irradiance into reflectance are detailed in Morel and Gentili,[9] and in Mobley.[10] The full set of these equations is also provided in the protocols for above- and in-water radiometry (described in Chapters 9 and 10 in Fargion and Mueller[8]). For the sake of completeness, those quantities and relationships needed here are briefly recalled below.

The spectral radiance emerging from the ocean, the so-called *water-leaving radiance*, is given by

$$L_W(\lambda, \theta, \phi \in \Omega_{\mathrm{FOV}}, \theta_s, 0^+) \tag{1}$$

which explicitly shows the angular dependencies of L_W on the radiance direction defined by the zenith angle θ, and the azimuth angle with respect to the sun direction, ϕ, ($\phi = 0$ for the sun's azimuth), and where Ω_{FOV} represents the solid angle of the detector centered on the direction (θ, ϕ). For a given detector, Ω_{FOV} is constant, and this argument is no longer repeated. The dependence on the illumination conditions prevailing above the sea surface is expressed in a simplified way by only introducing the solar zenith angle, θ_s. Actually, the situation is more complex, as the radiant field incident upon the surface includes a direct component from the sun and a diffuse component from the sky. In addition to the sun position in a cloudless sky, therefore, the aerosol nature and optical thickness determine the radiant field above the ocean, and then the upward radiance field inside the ocean. In the case of partly cloudy skies, the radiant field is more complex, because it depends on the cloud distribution.

At a depth z within the water, any upwelled radiance is denoted

$$L_u(\lambda, \theta', \phi, \theta_s, z), \tag{2}$$

where θ' is the nadir angle. Immediately beneath the surface, at a null depth denoted $z = 0^-$ by convention, this radiance will be partly reflected (or totally reflected if θ' exceeds the critical angle), and partly transmitted through the interface in a direction θ (zenith angle), given by Snell's law according to $\theta = \sin^{-1}(n \sin\theta')$, where n is the refractive index of sea water, so that

$$L_W(\lambda, \theta, \phi, \theta_s, 0^+) \; = \; T(\theta')\, L_u(\lambda, \theta', \phi, \theta_s, 0^-), \tag{3}$$

and for which $T(\theta')$ is the upward radiance transmittance through the interface and equals $n^{-2}[1 - \rho(\theta')]$, where $\rho(\theta')$ is the downward Fresnel reflectance coefficient corresponding to the slant upward direction[11] θ'. Note that for the wavelengths considered, n is essentially constant (so the ρ and, thus, the T values are essentially independent of λ).

The upward radiance is related to the upward irradiance, E_u, at the same depth (at 0^-, for example), through

$$L_u(\lambda, \theta', \phi, \theta_s, 0^-) \; = \; \frac{E_u(\lambda, \theta_s, 0^-)}{Q(\lambda, \theta', \phi, \theta_s, 0^-)}, \tag{4}$$

where the dimensionless bidirectional Q function is expressed in steradians (it would be exactly equal to π if the L_u field was isotropic). By introducing the irradiance reflectance, denoted R, E_u can be expressed as a function of the downward irradiance, E_d, just beneath the surface through

$$E_u(\lambda, \theta_s, 0^-) \; = \; R(\lambda, \theta_s)\, E_d(\lambda, \theta_s, 0^-). \tag{5}$$

When using an above-water method, the total radiance measured above the sea surface, L_T, includes the wanted information, i.e., L_W in Eq. (3), and a contamination term, ΔL, discussed later, originating from light reflected onto the sea surface and then into the sensor,

$$L_T(\lambda, \theta, \phi, \theta_s) \; = \; L_W(\lambda, \theta, \phi, \theta_s, 0^+) \; + \; \Delta L. \tag{6}$$

According to the latest version of the protocols[8] and simulations by Mobley,[10] θ is usually chosen between 20–50° (here 40°), and ϕ is generally between 90–135°, away from the sun's azimuth.

When using an in-water method, a vertical profile of L_u within the upper layer is determined with a radiometer pointed at nadir (θ' and $\phi = 0$). By using the appropriate attenuation coefficient (K_L), the $L_u(\lambda, 0, 0, \theta_s, 0^-)$ value at null depth is derived by extrapolating the profile toward the interface. This radiance is then propagated through the interface using Eq. (3), with T given the value $T(\theta' = 0) = T_0 = 0.546$, which has a nearly constant value regardless of the sea state,[10,11] so that

$$L_W(\lambda, 0, 0, \theta_s, 0^+) = 0.546\, L_u(\lambda, 0, 0, \theta_s, 0^-). \tag{7}$$

By assuming the unwanted term, ΔL in Eq. (6), has been successfully removed, the problem considered next is how best to intercompare the two determinations of L_W resulting from a simultaneous use of an above- an in-water method. By noting that for in-water measurements, θ, θ', and ϕ are all zero, Q in Eq. (4) takes a particular value, denoted $Q_n(\lambda, \theta_s, 0^-)$ (for the nadir viewing angle), which still depends on the sun position. For above-water measurements, the angular parameters θ', and ϕ in Eq. (4) are imposed by the pointing geometry of the sensor, and $T(\theta')$ may differ slightly from, and actually is always less than, the T_0 value. Making use of the superscripts "abw" and "inw" to represent the above- and in-water methods, respectively, the ratio of the L_W quantities is given by

$$\frac{L_W^{\mathrm{abw}}}{L_W^{\mathrm{inw}}} = \frac{T(\theta')}{T_0} \frac{Q_n(\lambda, \theta_s, 0^-)}{Q(\lambda, \theta', \phi, \theta_s, 0^-)}. \tag{8}$$

The remote sensing reflectance, R_{rs}, is defined as the ratio of the water-leaving radiance originating from nadir to the downward irradiance above the surface, $E_d(\lambda, \theta_s, 0^+)$:

$$R_{\mathrm{rs}}(\lambda, \theta_s) = \frac{L_W(\lambda, 0, 0, \theta_s, 0^+)}{E_d(\lambda, \theta_s, 0^+)}, \tag{9}$$

so it can be easily derived from the in-water radiance measurement. When using the above-water determination, some manipulations, as indicated by Eq. (8), are needed to obtain R_{rs} from L_W^{abw}:

$$R_{\mathrm{rs}}(\lambda, \theta_s) = \frac{L_W^{\mathrm{abw}}(\lambda, \theta, \phi, \theta_s, 0^+)}{E_d(\lambda, \theta_s, 0^+)} \frac{Q(\lambda, \theta', \phi, \theta_s, 0^-)}{Q_n(\lambda, \theta_s, 0^-)} \frac{T_0}{T(\theta')}. \tag{10}$$

Before transforming the signals into more elaborate quantities, such as $R_{\mathrm{rs}}(\lambda, \theta_s)$, it is first necessary to make sure the water-leaving radiances measured simultaneously but independently with both methods, are compatible within the desired accuracy, because ideally they must be equal. The so-called normalized water-leaving radiance[6,7] is a quantity used in particular when comparing field measurements to remote sensing prodits, and it is simply derived by multiplying the $R_{\mathrm{rs}}(\lambda)$ values by the extraterrestrial solar flux at the same wavelength.

3. Background and Goals

The SeaWiFS project goal of determining water-leaving radiances to within 5% uncertainties has been well demonstrated for in-water measurements in Case-1 waters,[12] but the uncertainties associated with above-water measurements have not been similarly assessed. This was the ultimate objective of the first SeaWiFS Bio-Optical Algorithm Round-Robin (SeaBOARR-98) experiment, which took place from 5–17 July 1998 at a tower in the northern Adriatic Sea, in shallow water near Venice.[13] The majority of the data were collected in Case-2 conditions, or close to the transition between Case-1 and Case-2 waters, according to the threshold defined by Loisel and Morel.[14]

The main difficulty with above-water methods is associated with correcting for the effects of surface waves, which introduce significant fluctuations into the glint and reflected skylight components of the above-surface radiance field. The problem is made more difficult by the presence of clouds. Some techniques attempt to reduce the negative effects of glint at the point of measurement,[15] but most methods deal explicitly with glint by filtering it out, or removing it with a more or less severe correction algorithm.

3.1 The Field Campaign

The *Productivité des Systèmes Océaniques Pélagiques* (PROSOPE) cruise was designed to study the productivity of pelagic oceanic systems as a contribution to the JGOFS-France Program. The campaign was on board the research vessel *Thalassa* (74.5 m length, 13.9 m breadth, and 6.2 m draught), and started in Agadir, Morocco, on 4 September 1999, and ended in Toulon, France, on 4 October. The cruise track began with a detailed study (3 days) in the productive upwelling zone off the northwest African coast, and ended within the much less productive Mediterranean Sea waters (Fig. 1a). The latter included 5-day studies of an ultra-oligotrophic regime in the Eastern Mediterranean (southwest of Crete) and a mesotrophic site in the Ligurian Sea (northwest of Corsica). In between the long-duration sites, nine daily stations were sampled over 4-hour periods centered around noon.

In addition to the usual determinations of JGOFS core parameters and other biochemical studies, extensive optical sampling was executed, particularly around and during the overpass of the SeaWiFS instrument. A part of this program was devoted to the upward radiance measurements, to the comparison of the above- and in-water methods, and to the evaluation of the difficulties associated with attaining the desired radiometric accuracy, specifically in the vicinity of a large sampling platform. Two in-water and one above-water system were used for these inquiries (Figs. 1b–1d, respectively): a) the Low-Cost NASA Environmental Sampling System (LoCNESS), b) the SeaWiFS Free-Falling Advanced Light Level Sensors (SeaFALLS), and c) the SeaWiFS Surface Acquisition System (SeaSAS).

The environmental conditions during the cruise were generally good, even exceptional in terms of sky condition and cloud cover, as well as in terms of the sea state and ambient wind (Table 1). The chlorophyll *a* data for the upper layer (everywhere Case-1 conditions) spanned two orders of magnitude (0.032–3.75 $mg\,m^{-3}$). The large range in chlorophyll *a* concentration, along with the diversity in optical measurements and the excellent environmental conditions, makes the PROSOPE data set well suited for investigating a variety of challenging bio-optical problems.

3.2 Objectives

The SeaBOARR-98 conclusions were based on three favorable days of useful data. From these data, four methods for correcting above-water observations intracompared at the 8% level, and they intercompared with three methods for processing the in-water data at the 9% level;[16] although, agreement at the 5% level was achieved in some circumstances, particularly when band ratios were compared rather than absolute quantities. The methods selected for the PROSOPE cruise are a subset of SeaBOARR-98 and will be described later. With the experience gained from the SeaBOAAR activity, the optical sampling objectives for the PROSOPE cruise were as follows:

1. Use two in-water profilers and one analysis method to compute water-leaving radiances from in-water data;
2. Use one above-water measurement system, and two surface glint correction methods to compute water-leaving radiances from above-water data; and
3. Use radiometers with a common calibration history to minimize intercalibration uncertainties.

In addition, the PROSOPE analysis plan was designed to overcome some deficiencies acknowledged during the SeaBOARR-98 experiment, in particular:

4. Intercompare the above- and in-water methods in Case-1 waters, and in deep ocean conditions;
5. Identify the origin, and quantify the significance of, perturbations caused by the sampling platform and environmental conditions on the surface radiance field;
6. Determine the effect of the orientation of the ship and the pointing angle of the instrumentation with respect to the sun's azimuth, and the direction of the ambient swell, when using the above-water method; and
7. Operate a correction scheme for including the bidirectional effects at the sea surface.

The magnitude of the perturbations in the proximity of a large structure is a recurring problem, which is made more complex according to the sun orientation with respect to the structure. These perturbations differentially influence the data obtained by the above- and in-water methods. For example, from the perspective of the in-water light field, investigations within 15–20 m of the aforementioned Venice tower have shown significant effects of the structure: approximately 3–8% for clear-sky conditions, and as much as 20% under overcast conditions.[17] Similar levels of uncertainties have been estimated for in-water measurements from a ship.[18]

For above-water measurements (recalling that the radiometer is never pointed into the ship's shadow), the perturbations are a combination of three possible effects: a) the shadow cast by the vessel outside the field of view of the sensor, but within the attenuation path lengths defined by the inherent water properties (shortest in the red, and longer in the other visible wavelengths); b) the interaction of the upward (in-water) radiant field with the submerged hull; and c) the interaction of the downward (above-water) radiant field with the exposed superstructure. For discussion purposes, the former is referred to as the *ship shadow* effect, the second interaction as the *hull albedo* effect, and the latter as the *superstructure albedo* effect.

4. Instrumentation and Sampling Procedures

All of the radiometers used with the optical sampling systems were built by Satlantic, Inc. (Halifax, Canada). Detailed descriptions of each instrument system have already been presented,[19] so only a brief description is given here. A summary of the wavelengths for each system is given in Table 2. LoCNESS and SeaSAS use 7-channel radiometers, 16-bit analog-to-digital converters, and are capable of measuring light over a 4-decade range. SeaFALLS includes 13 channels, 24-bit converters (and gain switching, which was not used during PROSOPE). These in-water instruments, equipped with buoyant fins at the tail and a weight near the nose, fall vertically through the water column as a rocket-shaped package with minimum tilts (less than 2°). Within the nose, LoCNESS has two sensors to measure the upward radiance and irradiance, $L_u(\lambda, z)$ and $E_u(\lambda, z)$, respectively, while SeaFALLS has only one sensor to measure $L_u(\lambda, z)$. Both profilers are configured with a downward irradiance, $E_d(\lambda, z)$, sensor located in the tail. They are also equipped with a conductivity-temperature probe, and a miniature fluorometer, to provide a basic physical and biological description of the water column (Figs. 1b and 1c).

Separate (one for each profiler), intercalibrated sensors measured the above-water total solar irradiance, $E_d(\lambda, 0^+)$; these reference sensors were mounted on masts on the top-most level of the ship's superstructure, completely free from any shading or reflecting obstacle. The profilers, connected by a 7 mm power and telemetry cable to the data acquisition systems, were deployed from the stern of the ship. They were floated approximately 30–50 m away, before being released for a free-fall profiling sequence, thereby avoiding any perturbations from the presence of the vessel.

The SeaSAS instrument includes two identical radiometers (with different saturation thresholds) which simultaneously and symmetrically measure the sky radiance reaching the surface, $L_{\mathrm{sky}}(\lambda)$, and the total radiance above the surface, $L_T(\lambda)$. The $L_{\mathrm{sky}}(\lambda)$ measurement is made by pointing the radiometer skyward at a zenith angle equal to the nadir angle of the $L_T(\lambda)$ observations (here $\theta = 40°$), and within the same azimuthal plane (away from the solar plane by at least 90°). This instrument system has an external module that measures the vertical (two-axis) tilts and horizontal (compass) pointing of the sensors (Fig. 1d). SeaSAS could not be accommodated on the bow of the vessel, so it was mounted on the port side above the bridge (and about 16.5 m above the water), with good surface viewing conditions in the azimuthal plane (±65° abeam). Under most circumstances, the heading of the vessel during the measurements was maintained in such a way that the bow or stern was approximately pointed toward the sun, to allow the radiometer to be easily pointed at least 90° away from the sun.

The basic data sampling procedure consisted of collecting data from all optical devices as simultaneously as possible. Hand-held radios were used to coordinate the deployments and operations, and constant communication was maintained with the bridge to ensure minimal heading deviations during the sampling intervals. The above-water sensors collected data in 3 min successive sequences, whereas the in-water profiler casts usually took 6–7 min (2–3 min for measurements during profiler descent, and then 3–4 min to pull the instruments back to the surface and ready them for another deployment). During stable atmospheric conditions, two SeaSAS casts were executed for each pair of in-water casts. All channels for all instruments were sampled within 167 ms, and all data were logged at full temporal resolution, to allow for subsequent optimal processing.

5. Data Processing

The in-water analysis techniques currently in use are based primarily on the Smith and Baker[20] method, hereafter referred to as S84. Variations in this method are derived from the measurement procedures (and platforms) used to acquire the data, and how the in-water data is propagated to the surface. Just as there are differing procedures for in-water data analysis, there are presently several methods for surface glint correction that were developed for different conditions in which above-water measurements are made (i.e., clear or cloudy sky, Case-1 or Case-2 conditions, etc.). The two methods applicable to the PROSOPE data set are Morel[21] and the so-called SeaWiFS Ocean Optics Protocols.[7,8] (hereafter, the former is referred to as M80 and the latter as S95, respectively).

5.1 In-Water (S84) Method

From the $L_u(\lambda, z)$ near-surface profiles, the attenuation coefficient $K_L(\lambda, z_0)$ is computed as the local (around the depth z_0) slope of $\ln[L_u(\lambda, z)]$. Then $K_L(\lambda, z_0)$ is used to extrapolate the upward radiance through the upper layer to determine $L_u(\lambda, 0^-)$ at null depth. The water-leaving radiance is then obtained using Eq. (7). Because there are two in-water sources, but only one processing method, the in-water data are distinguished by the measurement systems (*LN* or *SF* as superscripts for LoCNESS and SeaFALLS, respectively).

5.2 Above-Water (M80 and S95) Methods

The processing of above-water data consists of removing the contamination term, ΔL in Eq. (6), which adds to the marine signal and originates from reflections at the air–sea interface. The sky radiance reflected off the wave-roughened surface into the detector is *a priori* at the origin of the ΔL signal. As shown later on, however, reflected radiation from the sampling platform is another source of contamination. Even if only the sky reflection is considered, its contribution to L_T is always important. For Case-1 waters, in the near-infrared domain (e.g., at 780 and 865 nm) where the sea is *black*, this contribution amounts to 100%, and then decreases toward the short wavelength domain where the diffuse ocean reflectance departs from zero (see discussion below with Fig. 2). In Case-2 waters, particularly when the sediment load is high, the water reflectance may deviate from zero in the near infrared and the sky contribution remains less than 100%.

The M80 glint correction method is based on the existence of a black target in the near-infrared region. For all the PROSOPE data, 865 nm is the reference infrared wavelength, λ_r. The above-water radiance measured at λ_r is due entirely to surface reflection, and this estimate is extended over the whole spectrum by using the spectral dependence of the incident sky radiance, $L_{\rm sky}(\lambda)$, measured in the direction appropriate for reflection from the sea surface. Estimated glint is subtracted from the total signal to recover $L_W(\lambda)$, according to

$$L_W^{M80}(\lambda) \;=\; L_T(\lambda,\phi',\pi-\theta) \;-\; L_{\rm sky}(\lambda,\phi',\theta)\left[\frac{L_T(\lambda_r,\phi',\pi-\theta)}{L_{\rm sky}(\lambda_r,\phi',\theta}\right]. \tag{11}$$

It is important to note the following: a) in turbid Case-2 waters, the $L_W(\lambda_r) = 0$ assumption often fails and this method is not universally applicable (see Hooker et al.[16] for a case example); b) if other contaminating reflections play a part (such as those originating from the ship), they are captured when measuring $L_T(\lambda_r)$; and c) these other contaminations have a spectral composition which may (and generally do) differ from that of the sky used in Eq. (11), when the correction is extended throughout the visible spectrum.

The S95 method makes use of the same set of measurements, but they are used differently. The glint is removed through a constant interface reflectance factor, ρ, which is applied to the spectral sky radiances according to

$$L_W^{S95}(\lambda) \;=\; L_T(\lambda,\phi',\pi-\theta) \;-\; \rho(\lambda,\theta)L_{\rm sky}(\lambda,\phi',\theta). \tag{12}$$

The reflectance factor ρ would be the Fresnel reflectance averaged over the field of view of the detector pointed in the θ direction, Ω_{FOV}, if the interface was level. Generally, this is not the case, so ρ depends on the capillary wave slopes, and, thus, on wind speed. The wavelength dependence originates from the normal dispersion of the refractive index of water, which is weak and can be neglected. The ρ values result from theoretical considerations and simulations which account for the environmental conditions, i.e., slope statistics related to wind speed.[10,11] It is worth noting an extra source of reflected light (e.g., from the ship) is, by definition, assumed negligible when using the S95 method.

Above-water signals, as recorded in two contrasting situations, are shown in Fig. 2; also shown are examples of the spectral $L_W(\lambda)$ values, as retrieved by applying the M80 and S95 methods. Although the $L_T(\lambda)$ and $\rho L_{\mathrm{sky}}(\lambda)$ values converge at 865 nm, they do not converge exactly, and even less so at 780 nm; the $L_W(865)$ values, however, are practically the same in this instance, and close to zero. This is not always the case, as discussed later on.

Another important point is the variable contribution of $\rho L_{\mathrm{sky}}(\lambda)$ to $L_T(\lambda)$. In Fig. 2a, dealing with clear sky and blue oligotrophic water, the sky contribution in the visible part of the spectrum is maximal (about 40%) at 555 nm, and then decreases (about 20%) for blue (412–443 nm) radiation. In contrast, Fig. 2b corresponds to a situation with hazy overcast (but bright) sky and low reflecting chlorophyll-rich waters, and $\rho L_{\mathrm{sky}}(\lambda)$ represents about 75% of the total signal in the whole visible part of the spectrum. Note also that the incident solar irradiance peaks around 490 nm, so contamination from solar reflections (as can occur off the ship's superstructure, as discussed below) spectrally differs from reflected sky radiation, at least when the sky is not hazy and *whitish*.

5.3 Method Revisions

The Normalized Remote Sensing Reflectance (NRSR) workshop[13] (11–12 December 1997) established a baseline uncertainty for intercomparing $L_u(\lambda, z)$ profiles combined with above-water measurements of $E_d(\lambda, 0^+)$, of about 5% for $\lambda < 600$ nm, and $K_d(490) < 0.1\,\mathrm{m}^{-1}$. There was a consensus that comparative analyses should be restricted to this range of conditions, as well as low wind speed, $W < 10\,\mathrm{m\,s}^{-1}$, and a cloud cover less than 20%. The majority of the PROSOPE data were collected in low chlorophyll concentration waters in excellent environmental conditions: low wind speed ($W < 10\,\mathrm{m\,s}^{-1}$, except for one station), flat surface wave field, and generally clear skies (with occasionally some haze or scattered small cumulus clouds). Under such conditions, a large fraction of the data meets the restrictions for comparative analyses (the bold stations in Table 1).

The original specifications for S95 recommended a pointing angle $\theta = 20°$ from nadir.[7] Radiative transfer simulations above a wave-roughened surface from Mobley[10] showed a superior angle was 40°, and that a convenient azimuth angle was 135°. With these viewing angles, the reflectance factor ρ amounts to 0.028 for $W < 5\,\mathrm{m\,s^{-1}}$, and increases up to about 0.04 when $W = 15\,\mathrm{m\,s^{-1}}$. Except if otherwise stated, the reflectance $\rho = 0.028$ is always used in conjunction with the S95 method.

All of the above-water data were collected using common-sense procedures. In particular, foam and floating material were avoided, and no data collection was initiated unless the solar disc was unobscured by clouds (and expected to remain so for several minutes) and the sky within the field of view of the sky-viewing sensor was also cloud free. For some days, respecting these constraints required a considerable amount of time.

In reference to Eq. (6), the signal L_T actually results from the superposition of three contributions: a) the comparatively steady water-leaving radiance, L_W; b) the sky glint, and possibly other reflections, ΔL, usually slowly varying with the period of the waves and swell; and c) the mostly random, sharp, sun glint outliers produced by capillary waves when properly oriented with respect to the field of view of the above-water radiometer (even when the radiometer is pointed at least 90° away from the vertical solar plane, such flashes occur). The sun glint spikes are removed from the high frequency spectra, whereas the periodic variations of the sky glint are removed from the low frequency spectra. These removals require the use of appropriate filtering techniques.

Only the S95 method included a glint filter as part of the protocol. This filter plus eight others were evaluated by Hooker et al.[16] They concluded the most effective filter consisted of selecting the lowest 5% of the data in terms of radiance in the near-infrared bands, and then to use this selection as a temporal mask for all data at other wavelengths. This very high rejection rate (95%) was adopted for the processing of all PROSOPE data—this is an admittedly restrictive protocol, that is probably more severe than most of those in common use, often based on some averaging and less selective procedures.

5.4 Statistical Parameters

Three sources of $L_W(\lambda)$ estimates are available, two from in-water instruments and one from above-water measurements. Although a large number of casts were collected for each instrument, only data collected simultaneously by the three instruments are used in the following analyses to minimize any source of extraneous variance. No single method is presumed more correct than the other, so an unbiased percent difference (UPD), ψ_B^A, between two methods (A and B) providing $L_W(\lambda)$ estimates is defined as

$$\psi_B^A(\lambda_i) \; = \; 200\,\frac{L_W^A(\lambda_i) \; - \; L_W^B(\lambda_i)}{L_W^A(\lambda_i) \; + \; L_W^B(\lambda_i)}, \tag{13}$$

e.g., the UPD between the water-leaving radiances at 412 nm estimated with the M80 and S95 methods is $\psi_{S95}^{M80}(412)$.

The relative percent difference (RPD) between two data products is computed as:

$$\delta_B^A(\lambda_i) = 100 \frac{L_W^A(\lambda_i) - L_W^B(\lambda_i)}{L_W^B(\lambda_i)}. \tag{14}$$

For the RPD computations, the B method must be an appropriate *reference* value, and in this study, it is usually an in-water measurement.

Average percent differences, formed by binning the data over a subset of N casts are denoted by the so-called *bar* accent: $\bar{\delta}_{LN}^{S95}(412)$ are the average RPD values between $L_W^{S95}(412)$ and $L_W^{LN}(412)$ for a subset of the total (simultaneous) data set. Note that in all the percent differences, there is an implicit normalization with respect to the illumination conditions, because a ratio of radiance levels from two independent systems is always used.

6. Results

A large number of casts were collected for each instrument system (Table 1), but the desire here is to minimize any source of unnecessary variance, so the only data used in the analyses are for when the relevant instruments were collecting above- and in-water data simultaneously. Although theoretical[22] and empirical[23] studies of ship perturbations to the in-water light field are relevant, the primary perspective adopted here is with respect to above-water measurements collected from a large research vessel in low chlorophyll *a* concentration waters, under predominantly clear skies, and in Case-1 conditions.

6.1 In-Water Intracomparisons

Calibration stability over the course of a campaign is potentially an important source of variance in instrument comparisons involving individual channels.[12,24] For SeaWiFS field campaigns, the stability of the instruments is usually monitored with the SeaWiFS Quality Monitor (SQM). Unfortunately, using this instrument was not possible during PROSOPE, but the simultaneous deployment of two in-water profiling systems provides the possibility of comparing water-leaving radiances at all wavelengths from the two sensor systems over the entire cruise period.

The level of agreement between the two instruments during clear-sky conditions is presented in Fig. 3. The L_W values, regardless of wavelength, are well distributed with respect to the 1:1 line, and the histogram (inset panel) shows there is approximately a 2% bias between the two data sets. This agreement is very close to the uncertainty in the sensor calibration, estimated to be about 1.5–2.0%.[25] In spite of the absence of independent monitoring with the SQM, the performance of both sensor systems was very stable during the entire cruise period.

The number of clear-sky casts intracompared in Fig. 3 is 49, and they correspond to the number of SeaSAS casts which will be used later for an intercomparison of the above- and in-water methods (Sect. 6.3). Given the excellent agreement between the two in-water profilers, and the fact that the majority of the in-water sampling during clear-sky conditions was with the LoCNESS profiler, the L_W^{LN} values are hereafter considered as reference, or *sea-truth*, values.

6.2 Glint Correction Comparisons

As a consequence of the principles involved in their formulations, a comparison of the output of the M80 and S95 correction methods allows the detection of any ship contamination in the L_T signal. This is because the M80 method is sensitive to, and, thus, is able to identify a ship perturbation, whereas the S95 method, based on a theoretical value of the reflectance factor, will just ignore it. The presence of a ship perturbation can be detected with the ratio

$$r(865) = \frac{L_T(865)/L_{\rm sky}(865)}{\rho}, \tag{15}$$

where the numerator comes from M80 in Eq. (11) and the denominator from S95 in Eq. (12). Under normal circumstances, i.e., in the absence of a ship perturbation, $r(865) = 1$, within the accepted variance (and provided that ρ is given a correct value). Any other reflected radiation added to the sky-reflected radiation will lead to $r(865) > 1$, and the departure from unity is an estimate of this effect.

In Fig. 4, the $r(865)$ values are plotted as a function of α, i.e., the pointing angle of the above-water radiometers with respect to the perpendicular to the ship's center line. Although the total SeaSAS data set is composed of 137 casts (Table 1), 9 were excluded because of sampling problems (e.g., unanticipated cloud interference, ship movement during the cast, etc.). The remaining 128 casts provide a good distribution of data with respect to α, and show that when the instrument is pointed perpendicular to the side of the ship ($\alpha = 0$), the $r(865)$ values are a little larger than 1, which suggests a reduced contamination by the ship. As the radiometers are pointed more and more towards the bow or stern, that is when the distance of the surface spot away from the ship decreases, $r(865)$ dramatically increases, reaching values as high as 4–5 when $\alpha \approx \pm 60°$. These large ratios indicate the radiation reflected by the surface and seen by the sensor is largely dominated by that originating from the superstructure.

These high values, however, are not observed in a systematic manner. For example, when $\alpha = -40°$ or $-60°$, $r(865)$ values span the interval 1–5, which deserves another kind of analysis, involving γ, i.e., the angle between the center line of the ship and the position of the sun (Fig. 4 inset panel). According to the sign of γ, the port side of the ship (where the above-water radiometers were installed) is, or is not, illuminated by the sun, which makes a difference in the intensity (and spectral composition) of the light reflected from the superstructure. In Fig. 5, the

$r(865)$ values shown in Fig. 4 are plotted as a function of γ, and five categories of data in terms of binned α values are identified.

The first important observation from the Fig. 5 data is that $r(865)$ is close to 1 under an overcast sky, whatever the sun orientation. Under a clear sky, $r(865)$ remains not far from 1, when the sun is to starboard and the superstructure from which SeaSAS was operated is in shadow ($-120 > \gamma > -180°$). The converse holds true when the sun is to port ($120 < \gamma < 180°$), and the side of the ship where SeaSAS was measuring is directly illuminated. When γ is small, and the sun is almost aligned with the bow, the $r(865)$ values vary widely.

In conclusion, the contamination by the ship is reduced when the side from which the sensor is operated is in shadow, so that the superstructure is only illuminated by the sky radiation (or by uniform clouds); the contamination increases when the port side is sunlit, or if the bridge is sunlit (when γ is small). The geometrical aspect of the contamination is not surprising; more surprising is the importance of the effect and its complexity related to the superstructure shape. As with many ships, elements of the forward superstructure on *Thalassa wrapped around* to the sides of the vessel which provided reflection opportunities under a variety of sun geometries with respect to the bow.

From these results, it is possible to understand the limitations in intracomparisons between the S95 and M80 methods, because each is affected differently by the superstructure perturbation. At this point, Eq. (6) needs to be expanded (omitting the angular dependencies) as

$$L_T(\lambda) \;=\; L_W(\lambda) \;+\; \rho\, L_{\rm sky}(\lambda) \;+\; \Delta L_{\rm ship}(\lambda), \tag{16}$$

where ρ (already defined) applies to the sky radiance, $L_{\rm sky}(\lambda)$, and $\Delta L_{\rm ship}(\lambda)$ describes the radiance originating (i.e., reflected) from the ship's superstructure onto the water, and then reflected back into the sensor's field of view. In the S95 method, only $\rho L_{\rm sky}(\lambda)$ is subtracted from $L_T(\lambda)$, so this method produces an overestimate of the true $L_W(\lambda)$, because $\Delta L_{\rm ship}(\lambda)$ remains unquantified. With the M80 method, this term is known, but only at 865 nm; it is then propagated toward shorter wavelengths, using the spectral dependence of $L_{\rm sky}$. To the extent that the blue sky is bluer than the direct sunlight reflected by the superstructure (particularly if painted white), the extrapolation is wrong, which leads to an overestimate of $\Delta L_{\rm ship}(\lambda)$, and, thus, to an underestimate of $L_W(\lambda)$ at short wavelengths.

Figure 6 is a plot of the average relative differences between the M80 and S95 methods for each wavelength; data for clear-sky and overcast conditions are separately identified, as well as the data for the various $|\alpha|$ bins. Several aspects are worth noting:

1. As expected, the $L_W(\lambda)$ values derived from the M80 method are systematically less than those derived from the use of S95.

2. The overcast data show a minimal and spectrally constant difference (about 5%), because $\Delta L_{\text{ship}}(\lambda)$ is minimal in this case, and its spectral composition and that of L_{sky} are not much different. In these specific circumstances, the estimates via the M80 method would be the most accurate; by neglecting the ΔL_{ship} term, the S95 method would lead to a systematic overestimate of about 5%.

3. For the clear-sky data, the difference between the two methods is noticeable, even when $\alpha < 15°$, and increases when α and, thus, $\Delta L_{\text{ship}}(\lambda)$ increases; these differences exhibit a spectral shape, which will be discussed later (Sect. 6.4).

6.3 Above- and In-Water Intercomparisons

The in-water data are free from the perturbations due to the superstructure, and can be used to determine their magnitude. The intercomparison is made with a reduced data set composed of 49 casts (at 5 wavelengths), because a) the two types of measurements (above- and in-water) do not always overlap, and only those which are exactly coincident in time are kept; b) the above-water casts are restricted to clear sky conditions and $90 \leq \phi \leq 135°$; and c) the data with a pointing angle $|\alpha| > 45°$ are discarded, because there were only 4 simultaneous above- and in-water casts in this bin interval. Among the clear-sky data, only those corresponding to the most stable environmental conditions (and Mediterranean waters) are considered.

The intercomparison of L_W^{S95} (above-water, SeaSAS data, and the S95 method) and L_W^{LN} (in-water, LoCNESS data, and the S84 method), is made under these restrictions, and the results are presented in Fig. 7a. The above-water data are divided into two groups, those far from the ship ($|\alpha| \leq 15°$), and those closer to the ship ($15 < |\alpha| \leq 45°$). The inset panel displays the relative difference histograms, which shows that on average, the above-water data overestimate L_W (the δ values are positive); however, the δ values are better centered around zero if only the data acquired far away from the ship are considered. Note also the range of variance is fairly constant as a function of L_W (on either axis), so the biggest percent differences will be at 555 nm where the signal levels are lowest.

Because of the existence of bidirectional effects, the above- and in-water radiances are not directly comparable, and Eq. (8) must be included in the analysis. The above-water measurements made at $\theta = 40°$ (whence $\theta' = 29°$), can be transformed on a case-by-case basis as if they were made vertically ($\theta = 0°$). The transformation makes use of lookup tables derived from calculations for a clear sky, as discussed in Morel and Gentili.[9] Beside θ' and λ, the entries are ϕ, the azimuth difference (between the viewing and solar planes), and the chlorophyll concentration.

Because the PROSOPE measurements were often made around midday, the sun zenith angle (θ_s) was never very large (33–50°); such values, combined with ϕ between 90–135° and low chlorophyll concentrations (in the Mediterranean Sea), do not lead to a considerable bidirectional correction. The slant radiance slightly exceeds the nadir radiance, and the correction to be applied is about 0.967 ($\pm$0.0254 at 1 σ) for 412 nm, and 0.977 ($\pm$0.034 at 1 σ) at 555 nm. The corrected data are shown in Fig. 7b, with the associated histogram. Although it is not large, the movement of the points is in the correct direction, and the histogram shows a significantly stronger peak, with fewer outliers.

6.4 Spectral Intercomparisons

Figure 8 is a plot of $R_{\mathrm{rs}}^{S95}(\lambda)$ as a function of α; the remote sensing reflectance (not corrected for the Q-effect), is used to cancel out, in a simplified way, variations due to changing solar illumination. The data shown are only those for the Mediterranean Sea, with low chlorophyll concentration and clear-sky conditions. Consequently, the differences in $R_{\mathrm{rs}}^{S95}(\lambda)$ are rather weak, so the dependency of reflectance on α is not obscured by local differences, and the trends in Fig. 8 are significant. This figure shows the perturbation is characterized by the following:

1. There is a good symmetry with respect to $\alpha = 0$, which suggests rather homogeneous reflective properties of the superstructure, from the bow to the stern, when similarly lit;
2. As already noted, an increase in reflectance, actually in $\Delta L_{\mathrm{ship}}(\lambda)$, as a function of α; and
3. An increase of this perturbation as a function of λ; from weak, but detectable, levels at 412 nm, to large values (a factor of 5–10) in the infrared part of the spectrum.

These qualitative observations need to be reconciled with the varying proportions of the three components of the total surface signal in Eq. (16). The relative contribution of ΔL_{ship}, maximal when L_W is negligible (in the infrared part of the spectrum), progressively decreases as L_W increases (Fig. 2a) toward the blue end of the spectrum.

Table 3 and Fig. 9 present the $\bar{\delta}_{LN}^{S95}(\lambda)$ and $\bar{\delta}_{LN}^{M80}(\lambda)$ values as a function of the pointing angle $|\alpha|$ (in 15° bins). Both express, in terms of average values, the relative percent differences between above-water determinations (via the S95 or M80 methods), and the $L_W(\lambda)$ values derived from the in-water method (LN). For these blue waters, and when using the S95 method, the overall $L_W(\lambda)$ overestimate is rather small (less than 5%), except at 555 nm, where it reaches values as high as 14%, and even 25%, as a consequence of a lower marine signal at this wavelength (Fig. 3). When using the M80 method, the differences, almost spectrally neutral, are always negative, because of the overestimation of the $\Delta L_{\text{ship}}(\lambda)$ term (as previously noted).

Because band ratios are generally in use in ocean color algorithms[26], and sometimes as simplified measurements for sensor validation, the average differences between ratios derived from above-water measurements and those derived from in-water measurements are also displayed in Table 3. The large contamination of the 555 nm channel with the S95 method results in poor agreements for the three ratios considered (which all involve the 555 nm channel). In contrast, the almost equal overestimates, inherent with the M80 method, cancels out when forming the band ratios, so that the corresponding average differences remain small. This apparent agreement cannot be generalized, because it depends on the spectral composition of the superstructure albedo.

6.5 Ship Perturbation Correction

The perturbation effect is detectable through the use of the $r(865)$ ratio; its departure from unity forms a sensitive diagnostic parameter. Once detected, the next step is to examine whether a correction for this perturbation is possible with the available data. Although the complete reflective attributes of the ship's superstructure are unknown, a simplified correction scheme can be constructed at every wavelength using the superstructure reflection term in the infrared. This spectrally constant model is expressed as

$$\begin{aligned} \Delta L_{\text{ship}}(\lambda) &= \Delta L_{\text{ship}}(865) \\ &= L_T(865) - \rho L_{\text{sky}}(865). \end{aligned} \tag{17}$$

A spectrally dependent model of the superstructure contamination can also be constructed, which has something in common with that developped for the *residual term* mentioned in Fargion and Mueller[8] or in Toole et al.[27] This scheme actually rests on the assumption of a *white* reflection by a ship's superstructure illuminated by the sun and the sky. Under this assumption, $\Delta L_{\text{ship}}(\lambda)$ has the same spectral composition as $E_d(\lambda, 0^+)$, and is expressed as

$$\Delta L_{\text{ship}}(\lambda) = \left[L_T(865) - \rho L_{\text{sky}}(865)\right] \frac{E_d(\lambda, 0^+)}{E_d(865, 0^+)}. \tag{18}$$

The results of using these two correction schemes are presented in Table 4 (and to be compared with the S95 results, without correction, presented in Table 3). Whatever the scheme, the corrections result in lower $L_W^{LN}(\lambda)$ values, by a few percent for the 412–510 nm wavelengths, and more considerably at 555 nm, where the uncorrected values are significantly high (Fig. 9). The spectrally dependent model is more efficient than the constant model in correcting the 555 nm channel. With respect to in-water values, the relative differences, go from 20.6% (on average for uncorrected values, and when all α bins are pooled together) to 13.6% (spectrally constant correction), to 8.0% (wavelength-dependent correction).

Admittedly, the ship perturbation correction hypotheses underlying Eqs. (17) and (18) are questionable, although, the latter could be more realistic, if the superstructure painting was close to that of a neutral reflector (which remains to be verified). In summary, the results of the corrections are going in the right direction, without being fully satisfactory. To the extent that the 555 nm channel has not been fully corrected, the band ratios computed from the $L_W^{\rm abw}$ measurements remain inaccurate.

6.6 Oceanic Swell

One common feature of the oceanic environment that is not addressed in the protocols for above-water measurements is how to point the surface-viewing radiometer with respect to the ambient wave field. The possible importance of swell on deriving $L_W^{\rm abw}(\lambda)$ was partially quantified by Hooker et al.[16] who showed two above-water systems pointed opposite to one another with respect to the surface wave field, but still in keeping with the pointing requirements with respect to the sun, can differ (on average) by an additional 3–7% (during clear-sky conditions).

Multiple above-water systems were not deployed during PROSOPE, so the effects of surface gravity waves on the above-water measurements are addressed by splitting the 49 simultaneous above- and in-water casts into two groups: a) calm casts with no discernible swell (and, thus, no swell direction), and b) casts with a clear swell presence and direction. This produces a balanced data set, in terms of the number of $|\alpha|$ bins populated for each case: 22 bins for calm conditions and 27 for swell. Values of $\bar{\delta}_{LN}^{S95}(\lambda)$ were calculated for each group and each $|\alpha|$ bin, and then the calm values were subtracted from the swell values to produced a net percent difference (NPD).

The NPD values as a function of $|\alpha|$ (top half of Table 5) should be free of any common biases from ship perturbations (within reasonable limits associated with variability in the measurements, etc.), because the two data sets used in calculating the NPD values were binned separately. The $|\alpha|$ bins agree with one another to within approximately 2%, so there is no strong evidence of a sampling bias, although, the distribution of casts for each bin is not uniform. Remembering that the above-water radiances are (almost always) greater than the in-water radiances (Table 3), a net negative NPD value means the $L_W^{\rm abw}(\lambda)$ values in the presence of swell are lower than during calm conditions. Given this convention, there are important conclusions regarding the Table 5 (top half) results as a function of $|\alpha|$, particularly in comparison with the S95 results in Table 3:

1. The majority of the individual wavelengths have negative net difference values, which means the presence of swell results in lower above-water estimates of $L_W(\lambda)$; and
2. The depressive effect of swell is more accentuated at the 412 nm wavelength (independent of α), then it

diminishes at 443 nm, and becomes insignificant at the other wavelengths.

Note that as $|\alpha|$ increases beyond the first bin, the NPD values become more positive which indicates the variability of the ship perturbation (which will brighten the differences, on average, and make them more positive) is becoming greater. The exception is at 412 nm, where it is hypothesized the darkening is due to ship shadow, and at 555 nm where the ship perturbation is very large, so 1–2% differences are probably not significant.

Another aspect of the surface gravity wave field can be considered in relation to the angle β, i.e., the angle between the radiometer and the swell direction (Fig. 4 inset panel). If the radiometer is pointed in the same direction as the swell is moving towards, then $\beta = 0°$; if pointed in the opposite direction, $\beta = \pm 180°$. The data can be binned as a function of β to categorize the data in terms of the wave field (45° bins are used here): the sensor is viewing a) the wave crests moving away, $|\beta| \leq 45°$; b) along the wave troughs, $45 < |\beta| \leq 135°$; and c) the oncoming wave crests, $135 < |\beta| \leq 180°$. Again, the *calm data* are subtracted from the *swell data*, and the results (bottom half of Table 5) are as follows:

1. Measurements along the wave troughs are a significant local minimum, which means they are radiometrically darker than the wave crests at all wavelengths;
2. The darkening effect is the largest at 412 and 555 nm; and and
3. At 510–555 nm, the converse trend (i.e., a brightening) is also observed, when the crests are either oncoming or going away.

Note, the band ratio data appear to give a contradictory result, but this is not the case. The important point to remember is the 555 nm band is in the denominator, so it has an inverse relationship on the magnitude of the ratios (a decrease in the 555 nm band increases the ratio).

As noted before, the relative ship perturbation is the largest at 555 nm. Inasmuch as the magnitude of ΔL_{ship} interacts with the wave orientation, it is not surprising that the response of this channel is strongly effected (enhanced or depressed) by the swell orientation. It must be remembered, however, that the glint filter has, in principle, removed any signals artificially brightened by wave passage, because only the darkest 5% of the data are used for deriving $L_W^{\mathrm{abw}}(\lambda)$. In summary, the swell effects are significant, and complex in terms of the sampling geometry and spectral impact. Dedicated experiments are definitely needed to understand and properly account for these effects, which are not considered in the present above-water protocols.

Among other environmental conditions, cloudiness has been identified as having a potential effect (one conclusion of the NRSR workshop). If the excellent conditions in terms of cloud cover (CC in octa) with respect to the threshold

$CC < 3$ are compared to the remaining data, no systematic effect related to varying cloudiness was detected (apart from those described for hazy overcast conditions). Generally speaking, when a subsetting of the data is performed by applying the workshop criteria for excellent environmental conditions (the bold stations in Table 1), the results for $\delta_{LN}^{S95}(\lambda)$ and $\delta_{LN}^{M80}(\lambda)$ are mostly unchanged.

7. Conclusions

Although in-water measurements have been successful for deriving water-leaving radiances and validating ocean color sensors (the SeaWiFS sensor in particular), above-water measurements form an alternative, which remains to be comparatively evaluated. In terms of the primary effort, this was the first objective of this study, while the second one was to quantify the perturbations due to the sampling platform and environmental conditions on the above-water measurements.

Two independent but intercalibrated profiling instrument systems, both operated far from a large research vessel, provided the same results (within 2%) in terms of $L_W(\lambda)$, and satisfied the radiometric requirements under all conditions. The measurements were carried out in clear Case-1 waters under clear skies, so the extrapolation procedures were accurate and not degraded by instrument self-shading uncertainties. The in-water $L_W(\lambda)$ values can safely be (and were) used as reference values, to which the results of the above-water determinations, once corrected for the bidirectional dependency, were compared. By this way, the biases possibly affecting the latter were discerned.

To the extent that sun glint does not contaminate the above-water data (accomplished here using a high rejection rate of 95% of the brightest recorded data), removing the skylight reflection, or other kinds of reflections, is the major problem when processing the above-water measurements. In spite of excellent conditions, considerable effort, and a large number of sampling opportunities, the desired agreement between the above-water $L_W(\lambda)$ values and the in-water reference values (within $\pm 5\%$) was only achieved approximately half the time, and only for the S95 method: on 121 occasions (all wavelengths from 412–555 nm considered) out of 245 examined (whereas for the M80 method, agreement at the 5% level was achieved approximately 12% of the time). It is worth recalling that these 245 pairs of spectral data were originally sorted out of 310 available pairs (overcast and unstable solar illumination data were not intercompared).

Considering the flaws already identified when using above-water methods,[15,26] this rather low rate of success is not surprising, albeit somewhat discouraging, particularly when considering that more adverse (sea and sky) conditions are common. In rough sea states (without foam, however), the swell and its orientation are another source of complexity and inaccuracies, and can account for several percent of additional uncertainty (Table 5).

During PROSOPE (onboard *Thalassa*), the ship shadow and the hull albedo effects were significantly smaller, and appear mostly inseparable from, the perturbation related to the superstructure albedo. The main source of discrepancy between the above- and in-water determinations of water-leaving radiances, originates from the additional reflection by the ship's superstructure, which is generally poorly quantified, if not simply ignored. The use of two methods (S95 and M80) when processing the above-water data allowed the presence of this perturbation to be detected using a *diagnostic parameter*, the $r(865)$ ratio, and its departure from unity established the degree of contamination.

This ratio was found to be close to 1 in only a few occurrences (Figs. 4 and 5), which means superstructure contamination was the general rule in the present above-water measurements, and was considerable in some instances. Deriving this diagnostic parameter is an easy way to detect the presence of such contaminations (as well as any other unexpected contamination by any source brighter than the water itself), and this method can be recommended. Avoiding this ship contamination cannot be achieved through the use of polarizing systems, because its angular origin differs from that of the reflected sky radiation (and of the Brewster incidence angle). Correcting for this identified contamination is, in practice, extremely difficult, and attempts to do it proved to be rather inoperative (Table 4), in terms of achieving the SeaWiFS 5% radiometric objective. To develop a more efficient correction scheme, it will be necessary to know the spectral signature of the ship under various illumination conditions, which is practically an unsurmountable task.

If it is easily realized that the contamination affects the $L_W^{\mathrm{abw}}(\lambda)$ retrievals, a natural reaction is to believe band ratios are much less degraded. In other words, a sensor validation, or a vicarious calibration, based only on color ratios would be more accurate, and more easily successful. Unexpectedly, the present results have demonstrated the opposite. Although accurate $L_W^{\mathrm{abw}}(\lambda)$ values (via the S95 method) were occasionally obtained at three wavelengths (412, 443, and 490 nm), the band ratios remained severely affected, because of the failure in properly correcting the 555 nm channel, at least in blue waters, with a relatively low signal at this wavelength. For the same reason, correcting low signals typical of dark Case-2 waters is likely problematic.

Regarding the effect of surface gravity waves on the radiation field, their interaction with the superstructure reflections, and the varying magnitude of this effect with the wave orientation, the results presented here show a decrease in water-leaving radiance values often occurs in the presence of swell. A satisfactory explanation for this effect remains to be found, and specific studies under more controlled circumstances are needed. Such an effect, presently not corrected, is inevitable, and the choice of favorable viewing angles is generally very limited in field conditions. The spectral signature of superstructure reflections, however, suggests the contamination can be reduced if the surface-viewing radiometer is pointed along the wave troughs rather than into the wave crests (maintaining, of course, a perpendicular angle with respect to the side of the platform, i.e., $\alpha = 0°$).

From the evolution of the ship influence with increasing distance between the ship and the surface spot seen by the sensor (with decreasing α), it can be roughly inferred by extrapolation that the perturbation from *Thalassa* would have been avoided if the horizontal distance was approximately 18 m. For a pointing perpendicular to the side of the ship, and $\theta = 40°$, this would have required a sensor operated 21 m above the water. Beside the fact that this was not possible aboard *Thalassa*, such a mounting is not optimal, as the higher the instrument is mounted, the more it is negatively influenced by ship motion. Often, the largest opportunities for making choices about competing viewing requirements (sun, swell, and ship influence) come from sensors mounted or operated from the bow, at least when the vessel is not underway. The choice of the bow is not always possible, nor practical, because of pitching. In any case, each vessel is a particular case, and each day at sea with its specific wave orientation, cloudiness, ship heading, and sun position, is a separate challenge. Defining practical protocols cpable of coping with all these contengencies will be a difficult task.

These remarks emphasize the difficulties of above-water measurements, which are finally more difficult and demanding, and even more time consuming, than in-water measurements. Such measurements are perhaps inevitable in Case-2 waters, and also in Case-1 waters when performed from a ship of opportunity sailing without stopping. The allure is the still unproven possibility of getting reliable data with an acceptable yield from above-water measurements in various conditions. Consider, however, a scenario wherein an above-water system is mounted on a cargo vessel, or a ferry, with a fixed orientation, or hand held and operated by a sailor or even a scientist. If the system is fixed and autonomous, the data will be taken under largely unknown environmental conditions, and unfavorable geometries. If it is manually operated, within a limited amount of time and in the absence of corroborating information from other instruments, the problem remains about the same. It seems rather unlikely, therefore, that data with uncertainties below 5%, as required for meaningful calibration and validation activities, can be obtained by this way. Precise metrology, strict adherence to protocols, dedicated and sufficient ship time, and maybe improved instrumentation (miniaturized and gimballed, for example), are definitely needed to reach an accuracy commensurate with the requirements of vicarious calibation and algorithm validation.

Acknowledgments

The PROSOPE optical data set could not have been collected at the high level that was achieved without the unselfish contributions of H. Claustre and M. Babin. All of the optical data were acquired using software developed by J. Brown (University of Miami), and the in-water data were processed by S. Maritorena (University of California at Santa Barbara). Both persons have repeatedly contributed to the success of various components of the SeaWiFS field campaigns, and their initiative is greatly appreciated. The above-water data were processed by G. Lazin (Satlantic, Inc.) who also provided helpful comments on an early draft of the results. The final preparation of the manuscript benefitted from the editorial and logistical assistance of E. Firestone.

Appendix A

Glossary

CT Conductivity and Temperature

DATA-100 The power, telemetry, and analog-to-digital conversion unit for the Satlantic, Inc. series of instruments.

IOCCG International Ocean-Color Coordinating Group

JGOFS Joint Global Ocean Flux Study

LoCNESS Low-Cost NASA Environmental Sampling System

NASA National Aeronautics and Space Administration

NPD Net Percent Difference

NRSR Normalized Remote Sensing Reflectance (workshop held 11–12 December 1997)

PROSOPE *Productivité des Systèmes Océaniques Pélagiques* (productivity of pelagic oceanic systems)

SDY Sequential Day of the Year

RPD Relative Percent Difference

SeaBOARR SeaWiFS Bio-Optical Algorithm Round-Robin

SeaBOARR-98 The first SeaBOARR experiment (5–17 July 1998)

SeaFALLS SeaWiFS Free-Falling Advanced Light Level Sensors

SeaSAS SeaWiFS Surface Acquisition System

SeaWiFS Sea-viewing Wide Field-of-view Sensor

SQM SeaWiFS Quality Monitor

UPD Unbiased Percent Difference

Appendix B

Symbols

0^+ An altitude immediately above the sea surface.

0^- A depth immediately below the sea surface.

abw Used to denote an above-water method for determining water-leaving radiance, see Eq. (8).

C_a The chlorophyll a concentration.

CC The fractional cloud cover (in eighths).

$E_d(\lambda)$ The spectral downward irradiance.

$E_d(\lambda, 0^+)$ The total solar irradiance just above the sea surface.

$E_u(\lambda)$ The spectral upwelled irradiance.

H The wave height.

inw Used to denote an in-water method for determining water-leaving radiance, see Eq. (8).

$K_d(\lambda)$ The spectral diffuse attenuation coefficient calculated from $E_d(\lambda)$ profiles.

$K_L(\lambda)$ The spectral diffuse attenuation coefficient calculated from $L_u(\lambda)$ profiles.

$L_u(\lambda)$ The spectral upwelled radiance, see Eq. (2).

$L_{\rm sky}(\lambda)$ The sky radiance reaching the sea surface.

$\bar{L}_{\rm sky}(\lambda)$ A representative value of $L_{\rm sky}(\lambda)$.

$L_T(\lambda)$ The total spectral radiance immediately above the sea surface, see Eqs. (6) and (16).

$\bar{L}_T(\lambda)$ A representative value of $L_T(\lambda)$.

$L_W(\lambda)$ The spectral water-leaving radiance, see Eqs. (1), (3), and (7).

$L_W^{\rm abw}(\lambda)$ The spectral water-leaving radiance computed from above-water optical data.

$L_W^{\rm inw}(\lambda)$ The spectral water-leaving radiance computed from in-water optical data.

$L_W^{LN}(\lambda)$ The spectral water-leaving radiance computed from (in-water) LoCNESS optical data.

$L_W^{M80}(\lambda)$ The spectral water-leaving radiance computed using the Morel[21] method, see Eq. (11).

$L_W^{S95}(\lambda)$ The spectral water-leaving radiance computed using the SeaWiFS Ocean Optics Protocols[7,8] method, see Eq. (12).

$L_W^{SF}(\lambda)$ The spectral water-leaving radiance computed from (in-water) SeaFALLS optical data.

LN A code for indicating (in-water) LoCNESS data.

$M80$ A code for indicating above-water data processed using the Morel[21] method, see Eq. (11).

$n(\lambda)$ The refractive index of seawater.

N The number of casts in a data set or a partitioned subset.

N_c The number of casts in calm conditions.

N_s The number of casts in the presence of swell.

$Q(\lambda)$ The spectral bidirectional Q function, see Eq. (4).

$Q_n(\lambda)$ The spectral bidirectional Q function at the nadir viewing angle.

$r(865)$ A diagnostic variable for determining the amount of reflected (contamination) radiation at the sea surface, see Eq. 15.

$R(\lambda)$ The spectral irradiance reflectance, see Eq. (5).

$R_{\mathrm{rs}}(\lambda)$ The spectral remote sensing reflectance, see Eqs. 9 and 10.

$R_{\mathrm{rs}}^{S95}(\lambda)$ The spectral remote sensing reflectance calculated using the S95 method to derive the water-leaving radiance.

$S95$ A code for indicating above-water data processed using the SeaWiFS Ocean Optics Protocols[7,8] method, see Eq. 12.

SF A code for indicating (in-water) SeaFALLS data.

$T(\theta')$ The upward radiance transmittance through the sea surface.

T_0 A constant value for $T(\theta')$ (equal to 0.546).

W The wind speed.

z The vertical coordinate (depth or altitude).

z_0 The center of the in-water extrapolation interval.

α The amidships pointing angle of the SeaSAS instruments, see Fig. 4 (inset panel).

β The angle between the radiometer and the swell direction, see Fig. 4 (inset panel).

γ The angle between the center line of the ship and the position of the sun, see Fig. 4 (inset panel).

$\delta_B^A(\lambda_i)$ The RPD at center wavelength (channel) λ_i for two data products $L_W^A(\lambda_i)$ and $L_W^B(\lambda_i)$, where the A and B codes identify the methods or data sources used, see Eq. (14).

$\bar{\delta}_B^A(\lambda_i)$ The average of δ_B^A over N casts.

ΔL A contaminating radiance contribution, see Eq. (6).

$\Delta L_{\mathrm{ship}}(\lambda)$ The ship perturbation radiance contribution to the above-water radiance field, see Eq. 16.

θ The zenith angle.

θ' The nadir angle.

θ_s The solar zenith angle.

κ A (small) linear contamination coefficient to the total above-water radiance to parameterize the effect of a (reflective) ship perturbation.

λ Wavelength.

λ_i A center wavelength or channel.

λ_r A wavelength or channel in the near-infrared part of the spectrum.

ϕ The azimuth angle with respect to the sun direction ($\phi = 0$ for the sun's azimuth).

φ The tilt of a measurement platform with respect to the vertical axis.

ρ The Fresnel reflectance coefficient.

$\psi_B^A(\lambda_i)$ The UPD at center wavelength (channel) λ_i for two data products $L_W^A(\lambda_i)$ and $L_W^B(\lambda_i)$, where the A and B codes identify the methods or data sources used, see Eq. (13).

Ω_{FOV} The solid angle of a radiometer's detector centered on the direction (θ, ϕ).

REFERENCES

1 IOCCG, "Minimum requirements for an operational ocean-colour sensor for the open ocean," *Reports Int. Ocean-Colour Coord. Group, Rept. No. 1,* (Int. Ocean-Colour Coord. Group, Nova Scotia, Canada, 1998).

2 Hooker, S.B., and W.E. Esaias, "An overview of the SeaWiFS project," *Eos, Trans., Amer. Geophys. Union* **74,** 241–246 (1993).

3 McClain, C.R., W.E. Esaias, W. Barnes, B. Guenther, D. Endres, S. Hooker, G. Mitchell, and R. Barnes, "Calibration and validation plan for SeaWiFS," *NASA Tech. Memo. 104566, Vol. 3,* S.B. Hooker and E.R. Firestone, eds. (NASA Goddard Space Flight Center, Greenbelt, Maryland, 1992).

4 Hooker, S.B., and C.R. McClain, "The calibration and validation of SeaWiFS data," *Prog. Oceanogr.* **45,** 427–465 (2000).

5 McClain, C.R., M.L. Cleave, G.C. Feldman, W.W. Gregg, and S.B. Hooker, "Science quality SeaWiFS data for global biosphere research," *Sea Technol.* **39,** 10–15 (1998).

6 Mueller, J.L., and R.W. Austin, "Ocean optics protocols for SeaWiFS validation," *NASA Tech. Memo. 104566, Vol. 5,* S.B. Hooker and E.R. Firestone, eds. (NASA Goddard Space Flight Center, Greenbelt, Maryland, 1992).

7 Mueller, J.L., and R.W. Austin, "Ocean optics protocols for SeaWiFS validation, revision 1," *NASA Tech. Memo. 104566, Vol. 25,* S.B. Hooker, E.R. Firestone, and J.G. Acker, eds. (NASA Goddard Space Flight Center, Greenbelt, Maryland, 1995).

8 Fargion, G.S., and J.L. Mueller, "Ocean optics protocols for satellite ocean color sensor validation, revision 2," *NASA Tech. Memo. 2000–209966,* (NASA Goddard Space Flight Center, Greenbelt, Maryland, 2000).

9 Morel, A., and B. Gentili, "Diffuse reflectance of oceanic waters, III. Implication of bidirectionality for the remote sensing problem," *Appl. Opt.* **35,** 4,850–4,862 (1996).

10 Mobley, C.D., "Estimation of the remote-sensing reflectance from above-surface measurements," *Appl. Opt.* **38,** 7,442–7,455 (1999).

11 Austin, R.W., "The Remote Sensing of Spectral Radiance from Below the Ocean Surface," In: *Optical Aspects of Oceanography,* N.G. Jerlov and E.S. Nielsen, eds. (Academic Press, London, 317–344, 1974)

12 Hooker, S.B., and S. Maritorena, "An evaluation of oceanographic radiometers and deployment methodologies," *J. Atmos. Ocean. Technol.* **17,** 811–830 (2000).

13 Hooker, S.B., G. Zibordi, G. Lazin, and S. McLean, "The SeaBOARR-98 Field Campaign," *NASA Tech. Memo. 1999–206892, Vol. 3,* S.B. Hooker and E.R. Firestone, eds. (NASA Goddard Space Flight Center, Greenbelt, Maryland, 1999).

14 Loisel, H., and A. Morel, "Light scattering and chlorophyll concentration in case 1 waters: A reexamination," *Limnol. Oceanogr.* **43,** 847–858 (1998).

15 Fougnie, B., P-Y. Deschamp, and R. Frouin, "Vicarious calibration of the POLDER ocean color spectral bands using *in situ* measurements," *Trans. IEEE Trans. Geosci. Remote Sens.* **37,** 1,567–1,574 (1999).

16 Hooker, S.B., G. Lazin, G. Zibordi, and S. McLean, "An evaluation of above- and in-water methods for determining water-leaving radiances," *J. Atmos. Ocean. Technol.* submitted (2001).

17 Zibordi, G., J.P. Doyle, and S.B. Hooker, "Offshore tower shading effects on in-water optical measurements," *J. Atmos. Ocean. Tech.* **16,** 1,767–1,779 (1999).

18 Voss, K.J., J.W. Nolten, and G.D. Edwards, "Ship shadow effects on apparent optical properties," *Proc. Soc. Photo-Opt., Instrum. Eng.* Ocean Optics XII, **2,258,** 815–821 (1986).

19 Hooker, S.B., and G. Lazin, "The SeaBOARR-99 Field Campaign," *NASA Tech. Memo. 2000–206892, Vol. 8,* S.B. Hooker and E.R. Firestone, eds. (NASA Goddard Space Flight Center, Greenbelt, Maryland, 2000).

20 Smith, R.C., and K.S. Baker, "The analysis of ocean optical data," *Ocean Optics VII,* M. Blizard, ed., SPIE, **478,** 119–126 (1984).

21 Morel, A., "In-water and remote measurements of ocean color," *Bound.-Layer Meteorol.* **18,** 177–201 (1980).

22 Gordon, H.R., "Ship perturbation of irradiance measurements at sea 1: Monte Carlo simulations," *Appl. Opt.* **24,** 4,172–4,182 (1985).

23 Weir, C.T., D.A. Siegel, A.F. Michaels, and D.W. Menzies, "*In situ* evaluation of a ship's shadow," *Proc. Soc. Photo-Opt., Instrum. Eng.* Ocean Optics VIII, **637,** 186–190 (1994).

24 Hooker, S.B., and J. Aiken, "Calibration evaluation and radiometric testing of field radiometers with the SeaWiFS Quality Monitor (SQM)," *J. Atmos. Ocean. Tech.* **15,** 995–1,007 (1998).

25 Hooker, S.B., S. McLean, J. Sherman, M. Small, G. Zibordi, and J. Brown, "The Seventh SeaWiFS Intercalibration Round-Robin Experiment (SIRREX-7), March 1999," *NASA Tech. Memo. 2001–206892, Vol. 16,* S.B. Hooker and E.R. Firestone, eds. (NASA Goddard Space Flight Center, Greenbelt, Maryland, accepted, 2001).

26 O'Reilly, J.R., S. Maritorena, B.G. Mitchell, D.A. Siegel, K.L. Carder, S.A. Garver, M. Kahru, and C. McClain, "Ocean color chlorophyll algorithms for SeaWiFS," *J. Geophys. Res.* **103,** 24,937–24,953 (1998).

27 Toole, D.A., D.A. Siegel, D.W. Menzies, M.J. Neumann, and R.C. Smith, "Remote sensing reflectance determinations in the coastal ocean environment—impact of instrumental characteristics and environmental variability," *Appl. Opt.* **39,** 456–469 (2000).

Table 1. A summary of the average environmental conditions during the PROSOPE stations organized by the sequential day of the year (SDY): chlorophyll *a* concentration (C_a), wave height (H), wind speed (W), vertical tilt (φ), diffuse attenuation coefficient at 490 nm (K_d), solar zenith angle (θ_s), and cloud cover (CC). The *SF*, *LN*, and *SS* cast numbers refer to the SeaFALLS, LoCNESS, and SeaSAS systems, respectively. The station days and numbers in bold indicate excellent environmental conditions: $K(490) < 0.1\,\mathrm{m^{-1}}$, low wind speed ($W < 10\,\mathrm{m\,s^{-1}}$), flat surface wave field, and very clear skies (CC=0, 1, or 2). The station codes correspond to Fig. 1 as follows: "U" for the upwelling region off Agadir, "S" for the short daily stations, "M" for the very clear waters southwest of Crete, and "D" for the site northwest of Corsica; the numbers represent the serial encoding of the day-to-day sampling for each station type.

Station		*Cast Numbers*			C_a	H	W	φ	K_d	θ_s	CC	*Sky Conditions*
SDY	*No.*	*SF*	*LN*	*SS*	[mg m^{-3}]	[m]	[m s^{-1}]	[°]	[m^{-1}]	[°]	[1/8]	*During Sampling*
252	U1	1– 5			2.120	0.5	5.1		0.173	26.4	0	Clear w/haze
253	U2	6– 8	1– 4	1– 12	3.750	0.0	2.6	2.0	0.212	28.2	7	Hazy overcast
254	U3	9–11	5– 7	13– 19	1.570	0.5	5.1	1.0	0.120	30.3	7	Hazy overcast
255	**U4**	12–15	8–11	20– 23	0.650	0.5	8.2	1.2	0.070	27.0	0	Clear w/haze
258	**S2**	16–18	12–14	24– 26	0.085	1.0	8.7	2.0	0.025	34.6	2	Clear w/haze
259	S3	19–21	15–17	27– 28	0.063	0.5	5.7	1.7	0.028	38.4	4	Clear w/small clouds
260	S4	22–24	18–20	29– 33	0.049	0.0	4.6	1.4	0.028	35.8	6	Clear w/clouds
262	S6	25–28	21–25	34– 38	0.028	0.5	4.6	1.7	0.028	35.1	3	Clear w/clouds and haze
263	**M1**	30–33	26–28	39– 45	0.032	0.5	2.6	0.9	0.027	33.2	1	Clear w/haze
264	**M2**	34–37	29–32	46– 52	0.029	0.5	5.7	0.8	0.024	33.4	0	Clear w/haze
265	M3	38–40	33–35	53– 56	0.039	1.0	6.2	1.8	0.026	48.3	3	Clear w/clouds and haze
266	**M4**	41–44	36–39	57– 64	0.035	1.0	6.7	1.4	0.022	34.5	2	Clear w/haze
267	**M5**	45–47	40–42	65– 68	0.032	0.5	6.2	1.1	0.028	35.7	1	Clear w/haze
269	**S7**	48–51	43–46	69– 76	0.045	0.0	2.6	0.5	0.031	39.1	0	Clear w/haze
270	S8	52–54	47–49	77– 81	0.046	0.0	2.1	1.1	0.032	47.1	4	Clear w/clouds and haze
271	S9	55–57	50–52	82– 87	0.082	1.0	12.3	1.3	0.032	43.9	3	Clear w/small clouds
272	**D1**	58–60	53–67	88–109	0.112	0.0	7.2	1.2	0.044	48.1	0	Clear
273	D2	61–63	68–70	110–115	0.107	1.0	7.7	1.6	0.039	48.0	5	Clear w/clouds and haze
274	D3	64–66	71–78	116–130	0.096	0.5	3.6	2.1	0.040	49.2	4	Clear w/small clouds
275	D4	67–69	79–81		0.106	0.5	4.6		0.039	53.3	5	Clear w/clouds
276	D5	70–72	82–84	131–137	0.105	0.5	2.6	1.8	0.040	50.8	5	Thin cirrus

Table 2. Channel numbers (λ_i) and center wavelengths (in nanometers) for the radiometric sampling systems along with their primary physical measurement, in terms of their vertical sampling. All of the channels have 10 nm bandwidths. Bold values indicate channels common to all the instruments.

	SeaSAS (SS)			*LoCNESS (LN)*				*SeaFALLS (SF)*		
λ_i	$L_T(0^+)$	$L_{sky}(0^+)$	$E_d(0^+)$	$L_u(z)$	$E_d(z)$	$E_u(z)$	$E_d(0^+)$	$L_u(z)$	$E_d(z)$	$E_d(0^+)$
1	**412.7**	**412.6**	**412.2**	**411.6**	**411.3**	**411.4**	**411.9**	565.0	564.3	565.0
2	**443.1**	**442.4**	**443.0**	**442.7**	**442.5**	**442.7**	**443.0**	**411.8**	**411.1**	**411.7**
3	**489.5**	**491.3**	**489.6**	**489.9**	**489.3**	**490.0**	**489.8**	665.8	665.9	665.9
4	**510.1**	**510.3**	**511.0**	**510.3**	**509.1**	**509.3**	**511.0**	**443.0**	**442.9**	**443.2**
5	**554.8**	**554.1**	**554.2**	**554.2**	**554.8**	**554.3**	**555.5**	470.3	470.4	469.9
6	780.6	781.5	780.6	665.3	666.0	665.9	665.2	**489.3**	**489.2**	**489.9**
7	865.4	866.5	865.1	683.8	682.9	682.4	683.7	**510.4**	**511.0**	**510.3**
8								531.9	531.5	531.7
9								**554.8**	**555.3**	**554.4**
10								590.3	590.2	590.3
11								519.8	519.0	520.1
12								683.1	683.6	683.4
13								434.0	434.5	434.7

Table 3. A summary of the average RPDs between the above- and in-water estimates of water-leaving radiance in each $|\alpha|$ 15° bin, $\bar{\delta}_{LN}^{\text{abw}}(\lambda)$: $\bar{\delta}_{LN}^{S95}(\lambda)$ in the top half, and $\bar{\delta}_{LN}^{M80}(\lambda)$ in the bottom half. The three left-most columns present the band-ratio results. The number of casts in each $|\alpha|$ bin and for the overall data set is given by N.

Above-Water	$\lvert\alpha\rvert$ *Bin*	*Casts*	$\bar{\delta}_{LN}^{\text{abw}}(\lambda)$ [%]							
Method	*Interval* [°]	N	412	443	490	510	555	443/555	490/555	510/555
S95	$\lvert\alpha\rvert \le 15°$	14	0.7	0.5	−2.4	−2.5	14.4	−11.9	−14.5	−14.6
	$15° < \lvert\alpha\rvert \le 30°$	16	2.2	2.6	0.0	1.5	21.0	−14.8	−16.9	−15.8
	$30° < \lvert\alpha\rvert \le 45°$	19	1.1	2.5	0.4	3.4	24.8	−17.2	−19.0	−16.8
	Overall Average	*49*	*1.3*	*2.0*	*−0.5*	*1.1*	*20.6*	*−14.9*	*−17.0*	*−15.8*
M80	$\lvert\alpha\rvert \le 15°$	14	−8.8	−7.9	−10.3	−13.3	−5.7	−2.1	−4.5	−7.8
	$15° < \lvert\alpha\rvert \le 30°$	16	−12.8	−10.8	−12.6	−15.9	−10.9	0.6	−1.2	−5.0
	$30° < \lvert\alpha\rvert \le 45°$	19	−24.2	−19.3	−18.6	−21.4	−17.9	−1.5	0.1	−3.5
	Overall Average	*49*	*−16.1*	*−13.2*	*−14.3*	*−17.3*	*−12.1*	*−1.0*	*−1.7*	*−5.2*

Table 4. A summary of $\bar{\delta}_{LN}(\lambda)$ values for the spectrally constant (top half) and spectrally dependent (bottom half) ship perturbation correction schemes as a function of the $|\alpha|$ pointing angle (in 15° bins). The number of casts in each $|\alpha|$ bin and for the overall data set is given by N.

Correction Method	$\lvert\alpha\rvert$ *Bin Interval* [°]	*Casts* N	$\bar{\delta}_{LN}(\lambda)$ [%] 412	443	490	510	555	443/555	490/555	510/555
Constant	$\lvert\alpha\rvert \leq 15°$	14	−0.4	−0.6	−3.7	−4.6	9.5	−9.1	−11.9	−12.7
	$15° < \lvert\alpha\rvert \leq 30°$	16	0.5	1.0	−1.9	−1.7	13.8	−11.0	−13.5	−13.3
	$30° < \lvert\alpha\rvert \leq 45°$	19	−0.9	0.6	−1.9	−0.3	16.5	−13.3	−15.4	−14.2
	Overall Average	*49*	*−0.3*	*0.4*	*−2.4*	*−2.0*	*13.6*	*−11.3*	*−13.8*	*−13.5*
Dependent	$\lvert\alpha\rvert \leq 15°$	14	−1.0	−1.4	−4.9	−6.5	5.6	−6.5	−9.8	−11.4
	$15° < \lvert\alpha\rvert \leq 30°$	16	−0.4	−0.3	−3.7	−4.5	8.0	−7.5	−10.6	−11.4
	$30° < \lvert\alpha\rvert \leq 45°$	19	−1.9	−0.9	−4.0	−3.7	9.8	−9.5	−12.2	−12.1
	Overall Average	*49*	*−1.2*	*−0.8*	*−4.1*	*−4.8*	*8.0*	*−8.0*	*−11.0*	*−11.6*

Table 5. A summary of $\bar{\delta}_{LN}^{S95}(\lambda)$ values for the NPD analysis as a function of the $|\alpha|$ pointing angle (in 15° bins) and the $|\beta|$ swell angle (in 45° bins). The number of casts in calm conditions is given by N_c, and the number of casts in the presence of swell by N_s (the N_c and N_s values in the *Overall Average* rows are totals). Note that the majority of the swell data is for the above-water radiometer pointing down the wave troughs ($45° < |\beta| \leq 135°$), which is a consequence of the ship being preferentially pointed into the swell during station work.

Calculation Method	*Bin Interval* [°]	Casts N_s	Casts N_c	*Swell − Calm* $\bar{\delta}_{LN}^{S95}(\lambda)$ *Values* [%] 412	443	490	510	555	443/555	490/555	510/555
NPD	$\lvert\alpha\rvert \leq 15°$	9	5	−4.0	−2.4	−1.3	−1.0	−1.0	−2.0	−0.8	−0.3
	$15° < \lvert\alpha\rvert \leq 30°$	7	9	−4.2	−2.0	−0.6	−0.1	0.0	−1.6	−0.6	−0.3
	$30° < \lvert\alpha\rvert \leq 45°$	11	8	−4.3	−0.8	0.6	0.4	−2.4	−0.6	1.1	1.5
	Overall Average	*27*	*22*	*−4.1*	*−1.7*	*−0.4*	*−0.2*	*−1.2*	*−1.4*	*−0.1*	*0.3*
NPD	$\lvert\beta\rvert \leq 45°$	4		−2.3	−2.8	−2.7	0.6	5.3	−5.7	−4.9	−3.7
	$45° < \lvert\beta\rvert \leq 135°$	16		−5.3	−3.8	−3.4	−2.4	−6.1	1.8	2.7	2.1
	$135° < \lvert\beta\rvert \leq 180°$	7		−3.4	−1.6	−0.5	3.0	4.5	−3.4	−1.6	−0.5
	Overall Average	*27*	*22*	*−3.7*	*−2.8*	*−2.2*	*0.4*	*1.2*	*−2.5*	*−1.3*	*−0.7*

Figure Captions

Fig. 1. A schematic of the PROSOPE cruise sampling: **a)** the cruise track, with the short daily stations given by the (darkened) numbered bullets and the long multiday stations by the large circles (as encoded in Table 2); and the **b)** LoCNESS, **c)** SeaFALLS, and **d)** SeaSAS instrument systems. For the latter, the (open) numbered bullets identify common sensor types. All three measurement systems were equipped with sensors to measure the vertical tilt, φ, of the radiometers during sampling.

Fig. 2. Examples of spectral signals used when deriving water-leaving radiances, from the M80 and S95 methods, $L_W^{M80}(\lambda)$ and $L_W^{S95}(\lambda)$, respectively. Also shown are the downwelling irradiance, $E_d(\lambda, 0^+)$ (right-most vertical axis); the sky radiance, $L_{\rm sky}(\lambda)/10$ (scaled by a factor of 10, so the left-most vertical radiance axis does not have to be distorted); the reflected sky radiation, $\rho L_{\rm sky}(\lambda)$; and the total surface signal, $L_T(\lambda)$. Two contrasting environmental and sampling conditions are shown: **a)** measurements performed in very oligotrophic waters ($C_a = 0.035\,{\rm mg\,m^{-3}}$ on average) from the eastern-most part of the cruise track (days 263, 264, and 269, clear-sky conditions, and perpendicular viewing angles with respect to the side of the ship); and **b)** measurements from the upwelling zone off Agadir (day 253, hazy overcast conditions, $C_a = 3.750\,{\rm mg\,m^{-3}}$, and multiple viewing angles with respect to the side of the ship).

Fig. 3. The intracomparison of water-leaving radiances derived from the LoCNESS and SeaFALLS profilers, $L_W^{LN}(\lambda)$ and $L_W^{SF}(\lambda)$, respectively, during clear-sky conditions. The inset panel shows the histogram of $\psi_{LN}^{SF}(\lambda)$ values. The thin diagonal lines show the radiometric extent of the water-leaving radiances for the five blue-green wavelengths.

Fig. 4. The distribution of $r(865)$ as a function of α (negative α values are towards the stern and positive α values towards the bow). The total data set is composed of 128 casts: 19 were in overcast conditions and 109 were in clear-sky conditions. Overcast data are not shown as separate symbols, because they fall within a narrow range (slightly larger than 1) and all at $\alpha = 0$, so they would obscure the clear-sky results. The inset panel shows the pointing angle of the above-water radiometers with respect to the side of the ship (α) as well as the ambient swell (β), and the angle of the sun with respect to the bow (γ).

Fig. 5. The distribution of $r(865)$ as a function of γ (negative γ values are towards starboard and positive α values towards port as shown in Fig. 4). The total data set is the same as in Fig. 4, except overcast data are shown as the solid symbols, and the clear-sky data as open symbols. All the data are binned as a function of $|\alpha|$ (in 15° bins).

Fig. 6. The distribution of the average RPD values between the M80 and S95 methods, denoted $\bar{\delta}_{S95}^{M80}(\lambda)$, for clear-sky (open symbols) and overcast (closed symbols) conditions. The dashed line represents an average underestimation of M80 with respect to S95 of -5%.

Fig. 7. The intercomparison of above- and in-water estimates of $L_W(\lambda)$ during clear-sky conditions. The former are derived from the LoCNESS data, $L_W^{LN}(\lambda)$, and the latter using **a)** SeaSAS data with the S95 method, $L_W^{S95}(\lambda)$, and **b)** SeaSAS data with the S95 method plus the bidirectional (Q-factor) correction, $L_W^{Q95}(\lambda)$. The inset panels show the histograms of RPD values between the above- and in-water methods. The total data set is composed of 49 casts which are separated into two groups (14 and 35 casts, respectively): $|\alpha| \leq 15°$ (solid circles and dark gray bars), and $|\alpha| > 15°$ (open circles and light gray bars).

Fig. 8. The distribution of $R_{rs}^{S95}(\lambda)$ as a function of α for clear-sky conditions . Only five wavelengths are shown for clarity (the 443 and 490 nm data fall in between the 412 and 510 nm data).

Fig. 9. A comparison of average RPDs between in-water estimates of $L_W(\lambda)$ (from LoCNESS) and above-water estimates derived from the M80 (open symbols) and S95 (solid symbols) methods as a function of $|\alpha|$ during clear-sky conditions (49 casts). The dashed lines indicate the $\pm 5\%$ difference limits.

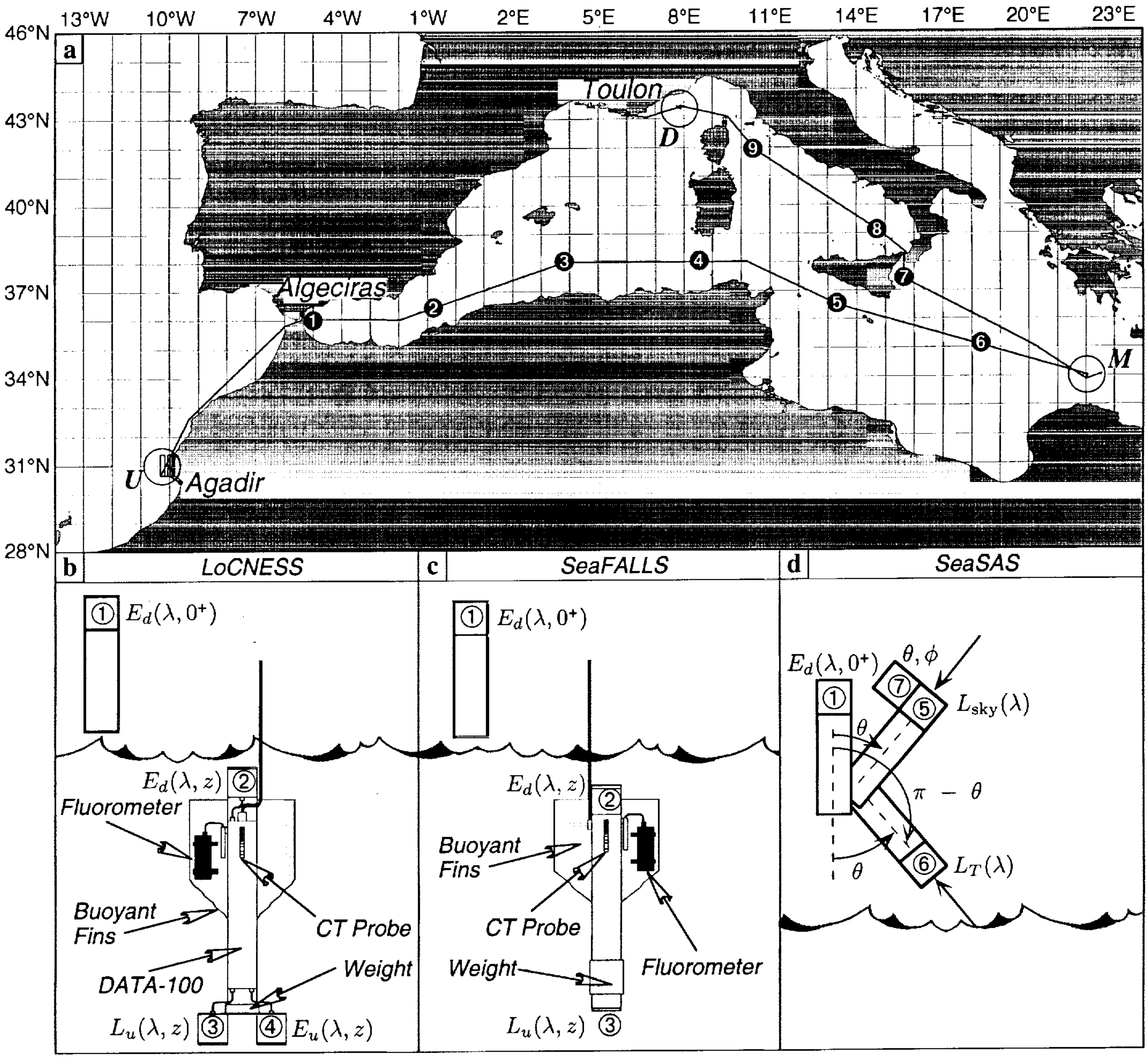
13°W
10°W
7°W
4°W
1°W
2°E
5°E
8°E
11°E
14°E
17°E
20°E
23°E
46°N
43°N
40°N
37°N
34°N
31°N
28°N
a
Toulon
D
Algeciras
M
U
Agadir
b
LoCNESS
c
SeaFALLS
d
SeaSAS
$E_d(\lambda, 0^+)$
$E_d(\lambda, z)$
Fluorometer
Buoyant Fins
CT Probe
DATA-100
Weight
$L_u(\lambda, z)$
$E_u(\lambda, z)$
$L_{sky}(\lambda)$
$L_T(\lambda)$
θ, ϕ
$\pi - \theta$

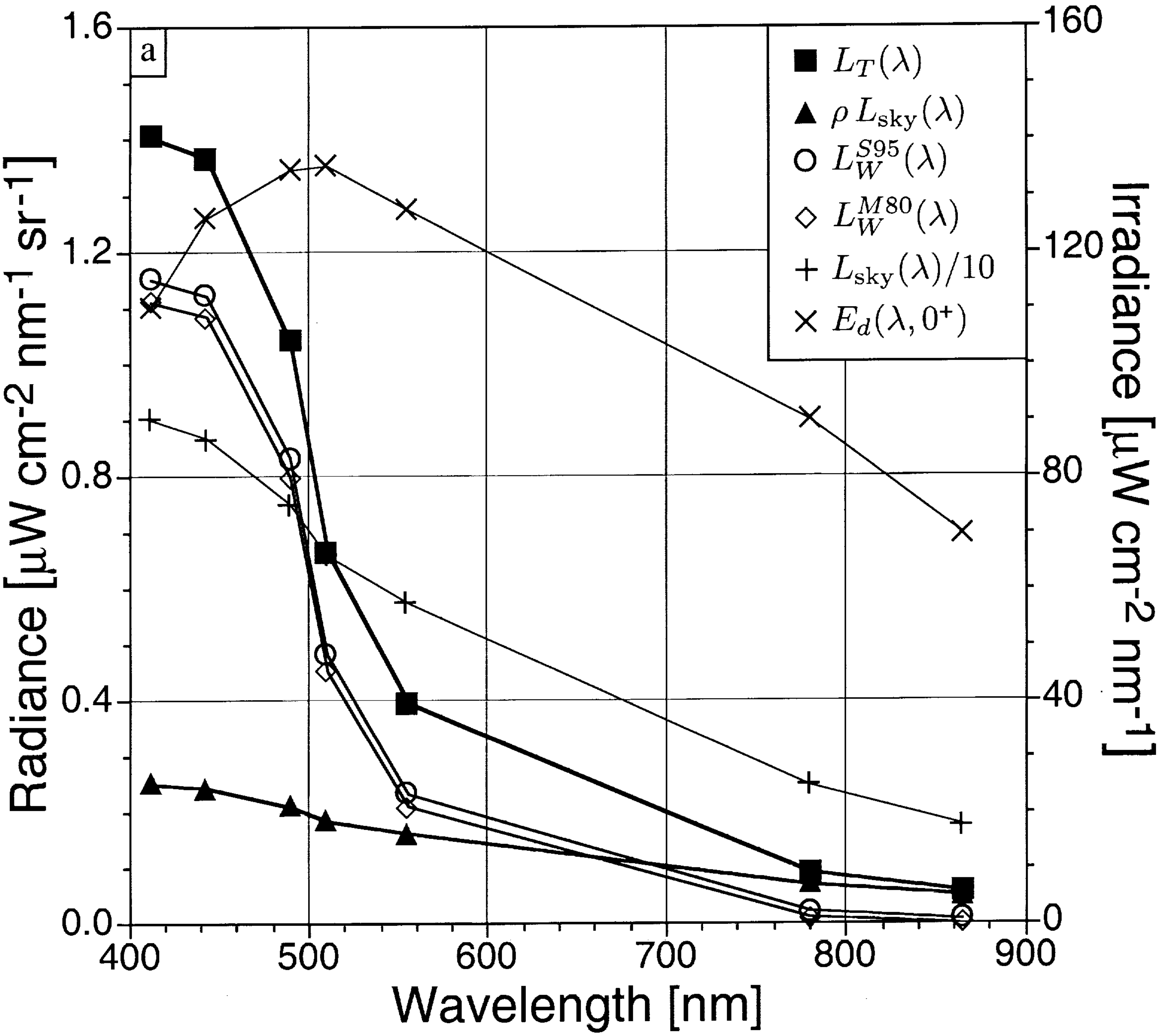
a
$L_T(\lambda)$
$\rho L_{sky}(\lambda)$
$L_W^{S95}(\lambda)$
$L_W^{M80}(\lambda)$
$L_{sky}(\lambda)/10$
$E_d(\lambda, 0^+)$
Radiance [µW cm-2 nm-1 sr-1]
Irradiance [µW cm-2 nm-1]
Wavelength [nm]
0.0
0.4
0.8
1.2
1.6
0
40
80
120
160
400
500
600
700
800
900

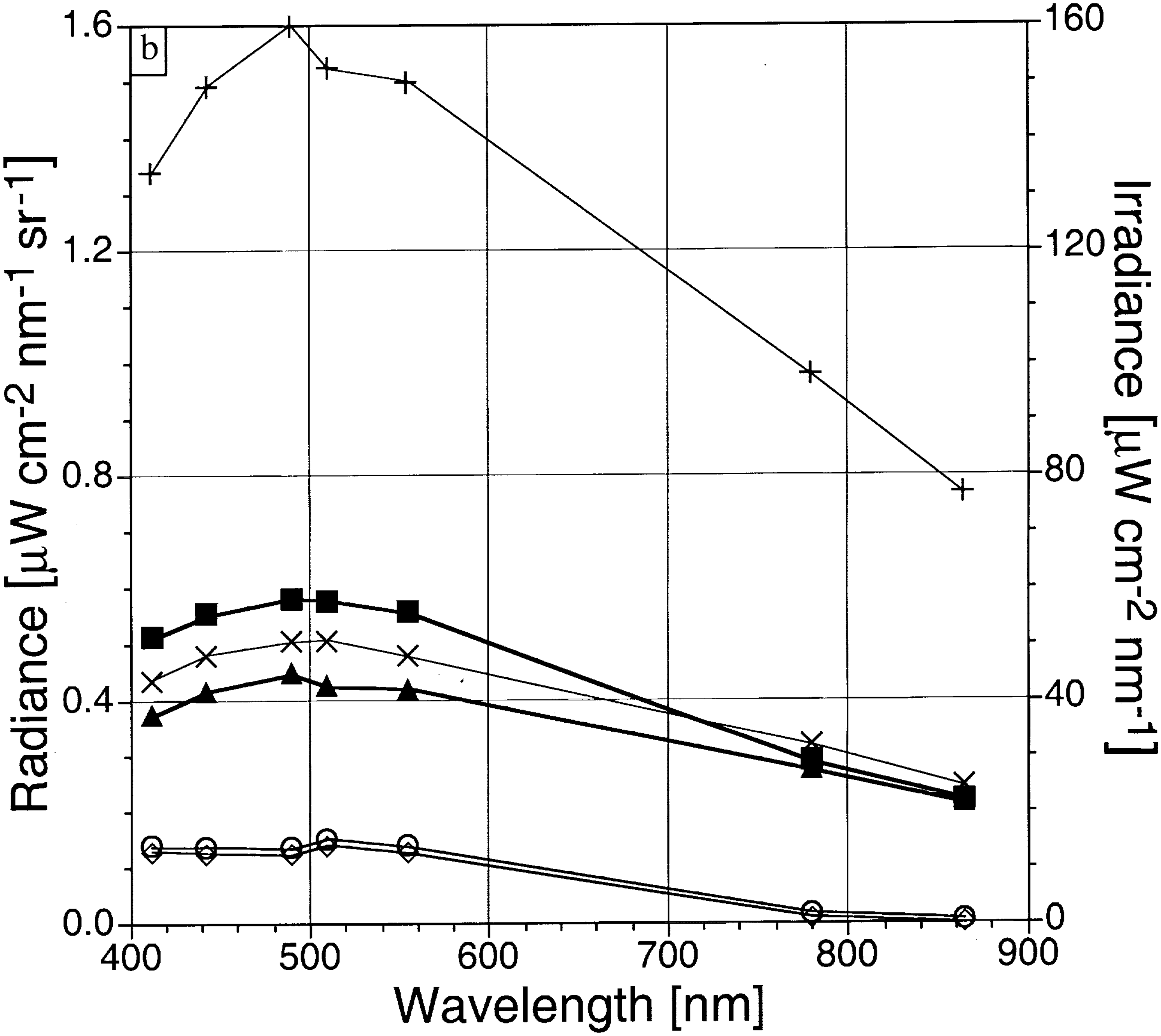
b
1.6
1.2
0.8
0.4
0.0
160
120
80
40
0
400
500
600
700
800
900
Radiance [μW cm-2 nm-1 sr-1]
Irradiance [μW cm-2 nm-1]
Wavelength [nm]

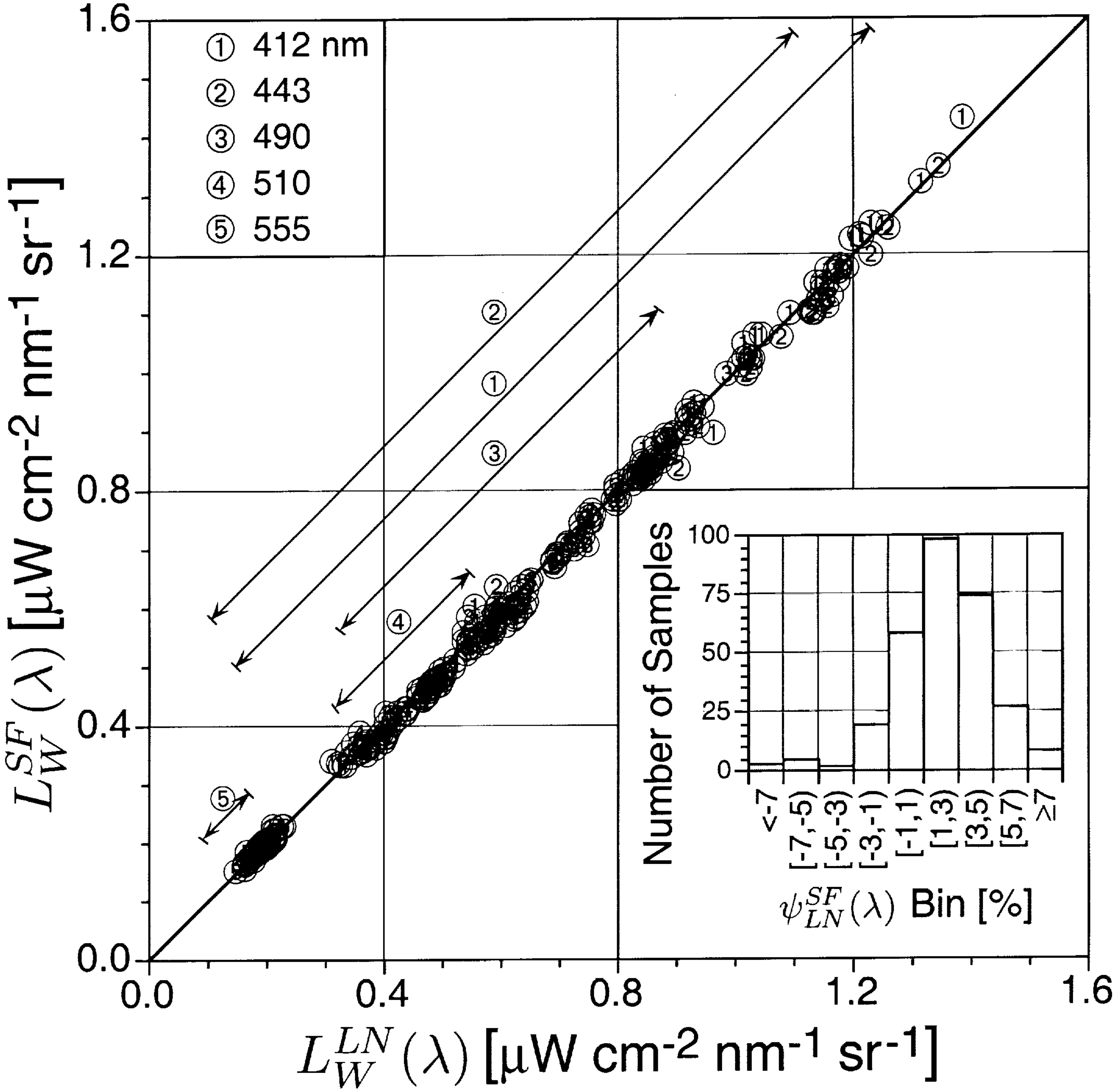
① 412 nm
② 443
③ 490
④ 510
⑤ 555
1.6
1.2
0.8
0.4
0.0
$L_W^{SF}(\lambda)$ [µW cm^{-2} nm^{-1} sr^{-1}]
$L_W^{LN}(\lambda)$ [µW cm^{-2} nm^{-1} sr^{-1}]
Number of Samples
100
75
50
25
0
<-7
[-7,-5)
[-5,-3)
[-3,-1)
[-1,1)
[1,3)
[3,5)
[5,7)
≥7
$\psi_{LN}^{SF}(\lambda)$ Bin [%]

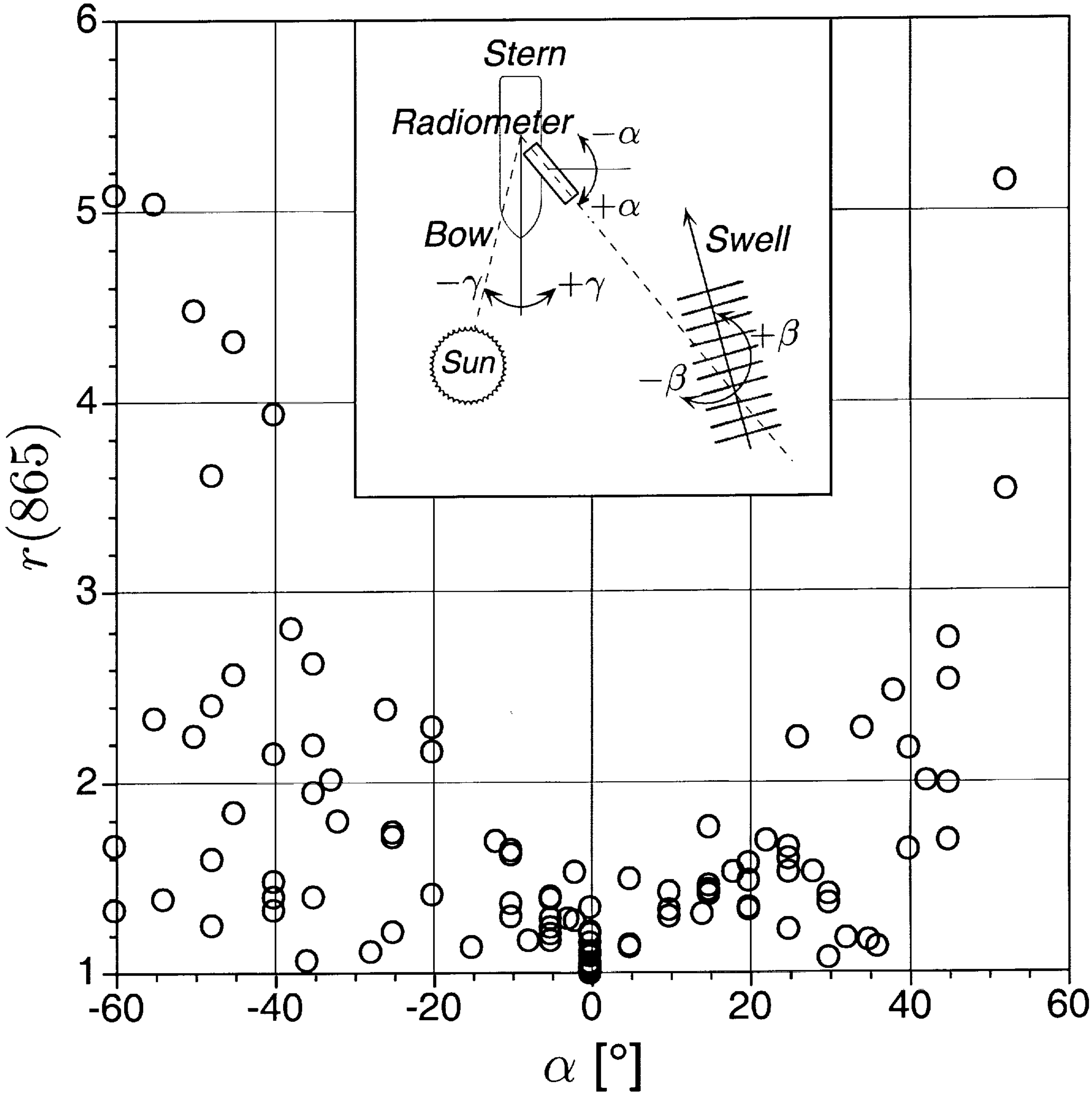
Stern
Radiometer
$-\alpha$
$+\alpha$
Bow
Swell
$-\gamma$
$+\gamma$
Sun
$+\beta$
$-\beta$
$r(865)$
α [°]
6
5
4
3
2
1
-60
-40
-20
0
20
40
60

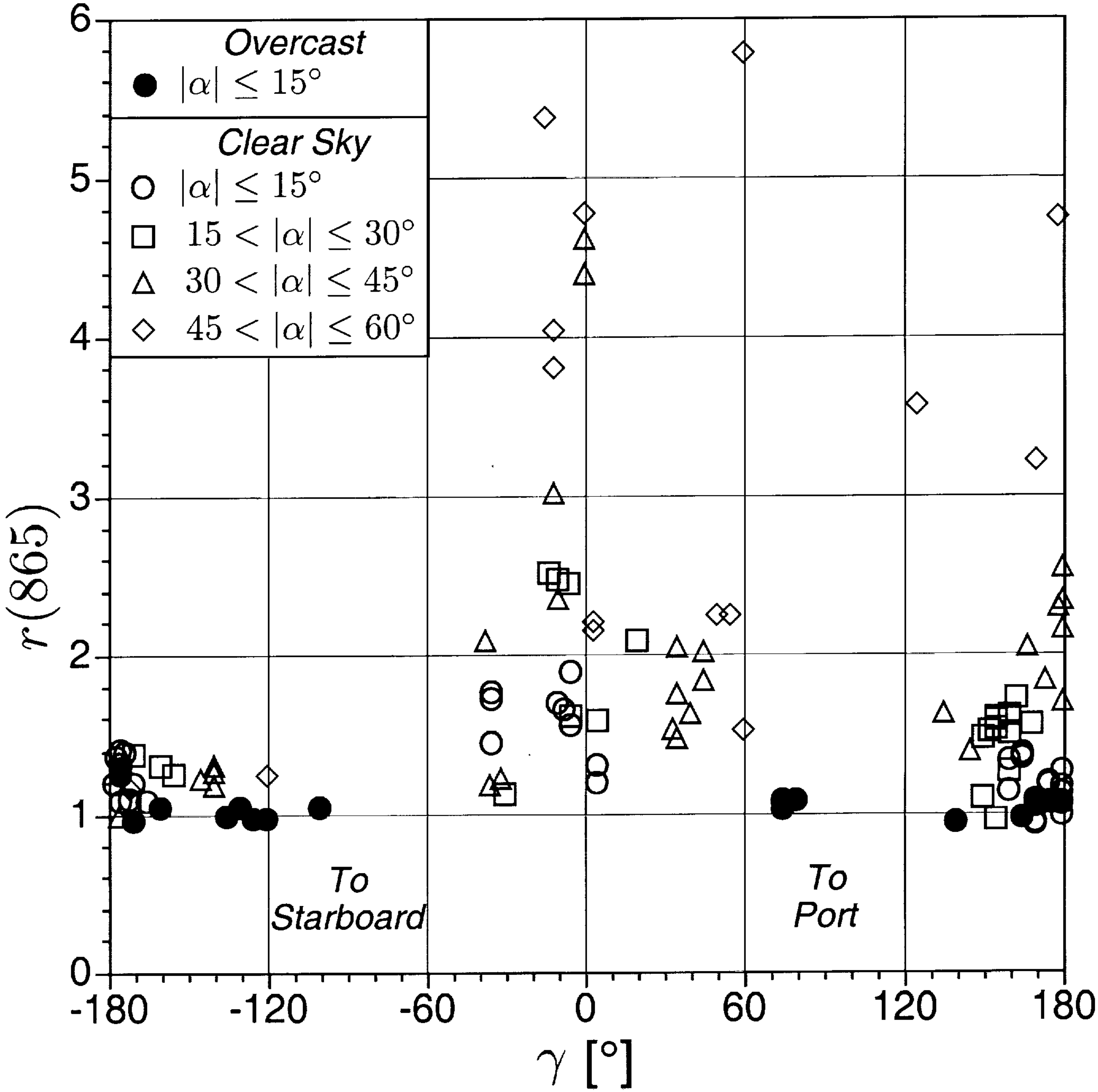
Overcast
$|\alpha| \leq 15°$
Clear Sky
$|\alpha| \leq 15°$
$15 < |\alpha| \leq 30°$
$30 < |\alpha| \leq 45°$
$45 < |\alpha| \leq 60°$
To Starboard
To Port
$r(865)$
γ [°]
0
1
2
3
4
5
6
-180
-120
-60
0
60
120
180

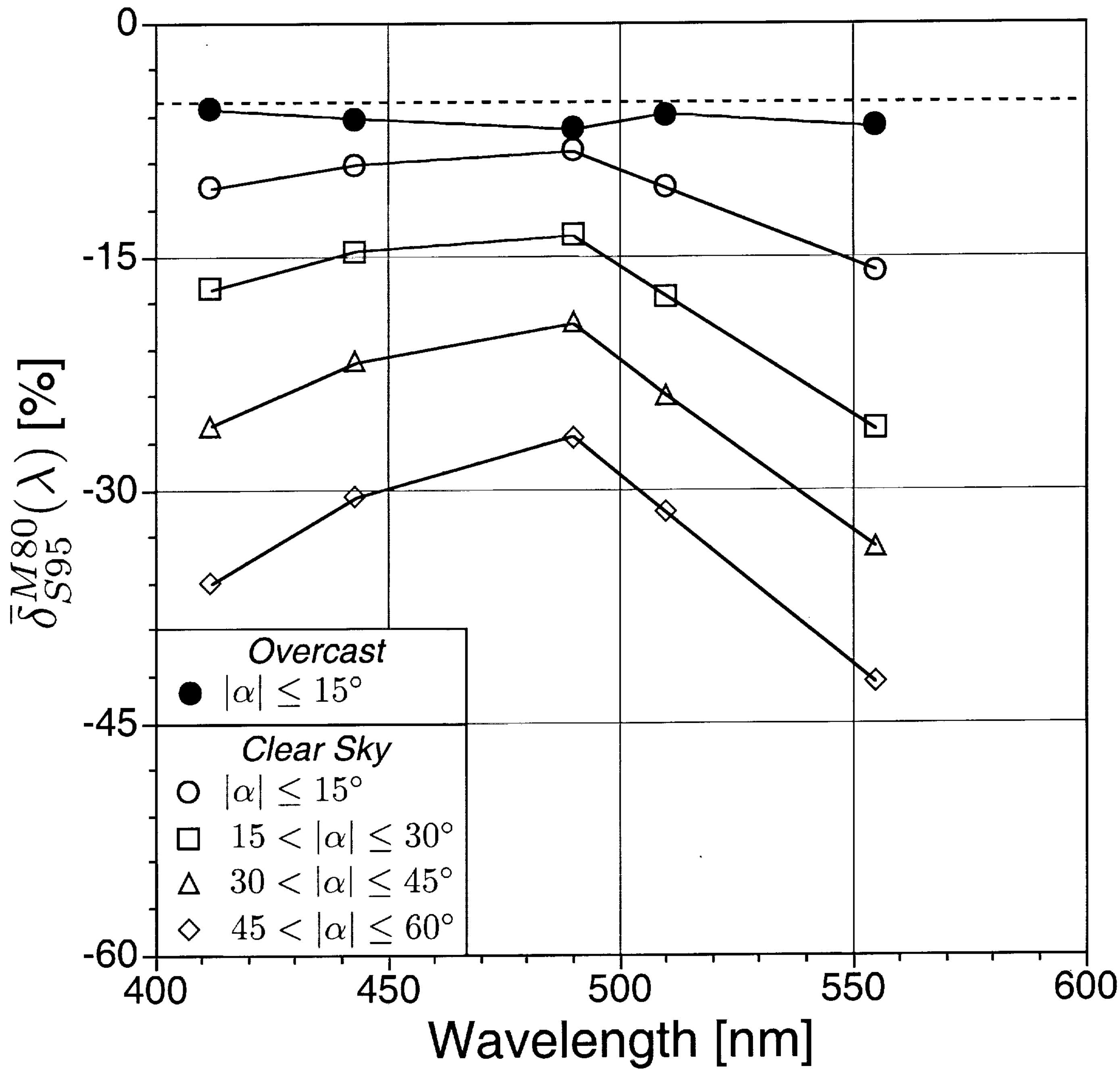
0
-15
-30
-45
-60
400
450
500
550
600
Wavelength [nm]
$\bar{\delta}_{S95}^{M80}(\lambda)$ [%]
Overcast
$|\alpha| \leq 15°$
Clear Sky
$|\alpha| \leq 15°$
$15 < |\alpha| \leq 30°$
$30 < |\alpha| \leq 45°$
$45 < |\alpha| \leq 60°$

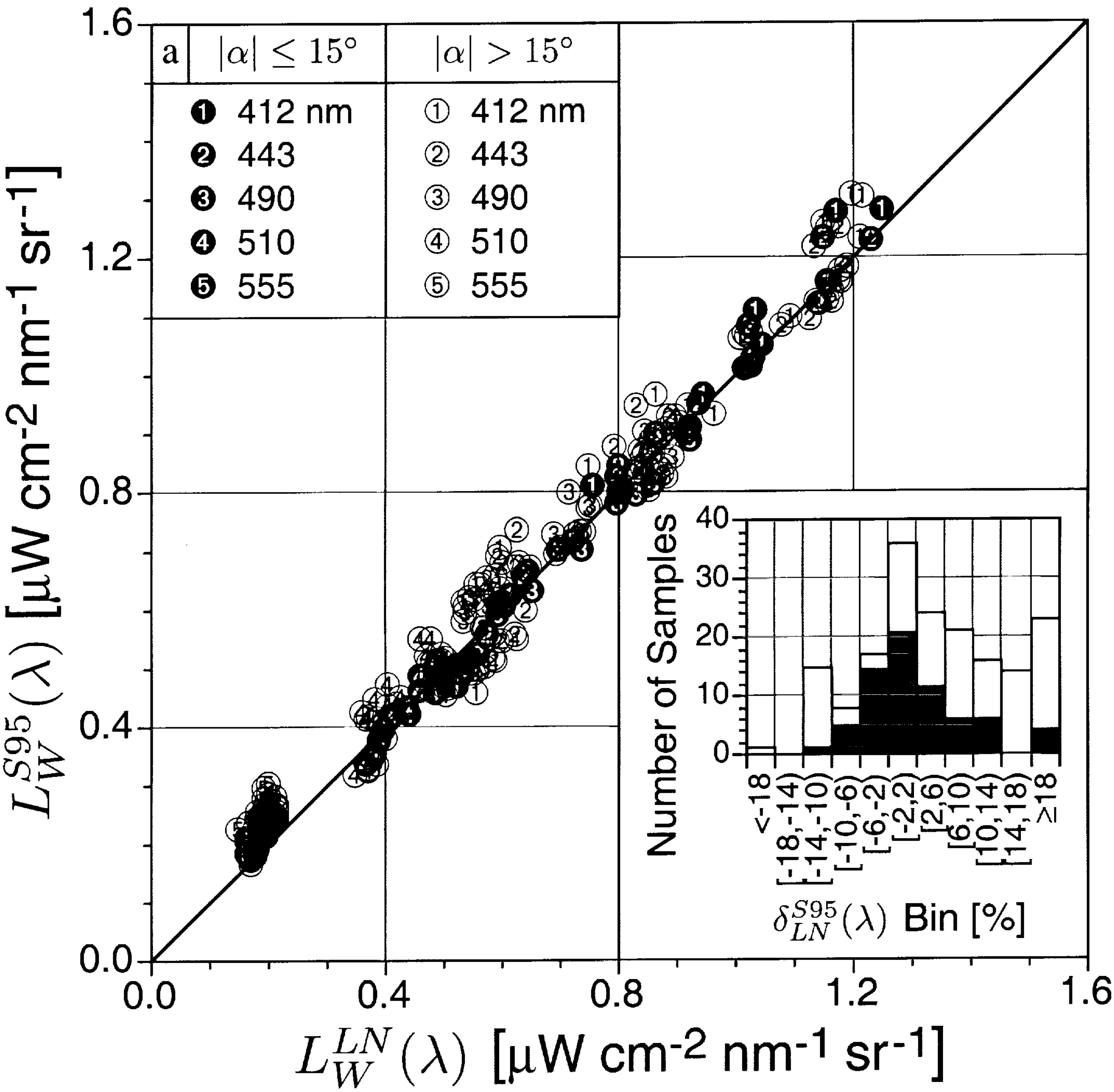
a
$|\alpha| \leq 15°$
$|\alpha| > 15°$
412 nm
443
490
510
555
412 nm
443
490
510
555
1.6
1.2
0.8
0.4
0.0
0.0
0.4
0.8
1.2
1.6
$L_W^{S95}(\lambda)$ [µW cm-2 nm-1 sr-1]
$L_W^{LN}(\lambda)$ [µW cm-2 nm-1 sr-1]
Number of Samples
40
30
20
10
0
<-18
[-18,-14)
[-14,-10)
[-10,-6)
[-6,-2)
[-2,2)
[2,6)
[6,10)
[10,14)
[14,18)
≥18
$\delta_{LN}^{S95}(\lambda)$ Bin [%]

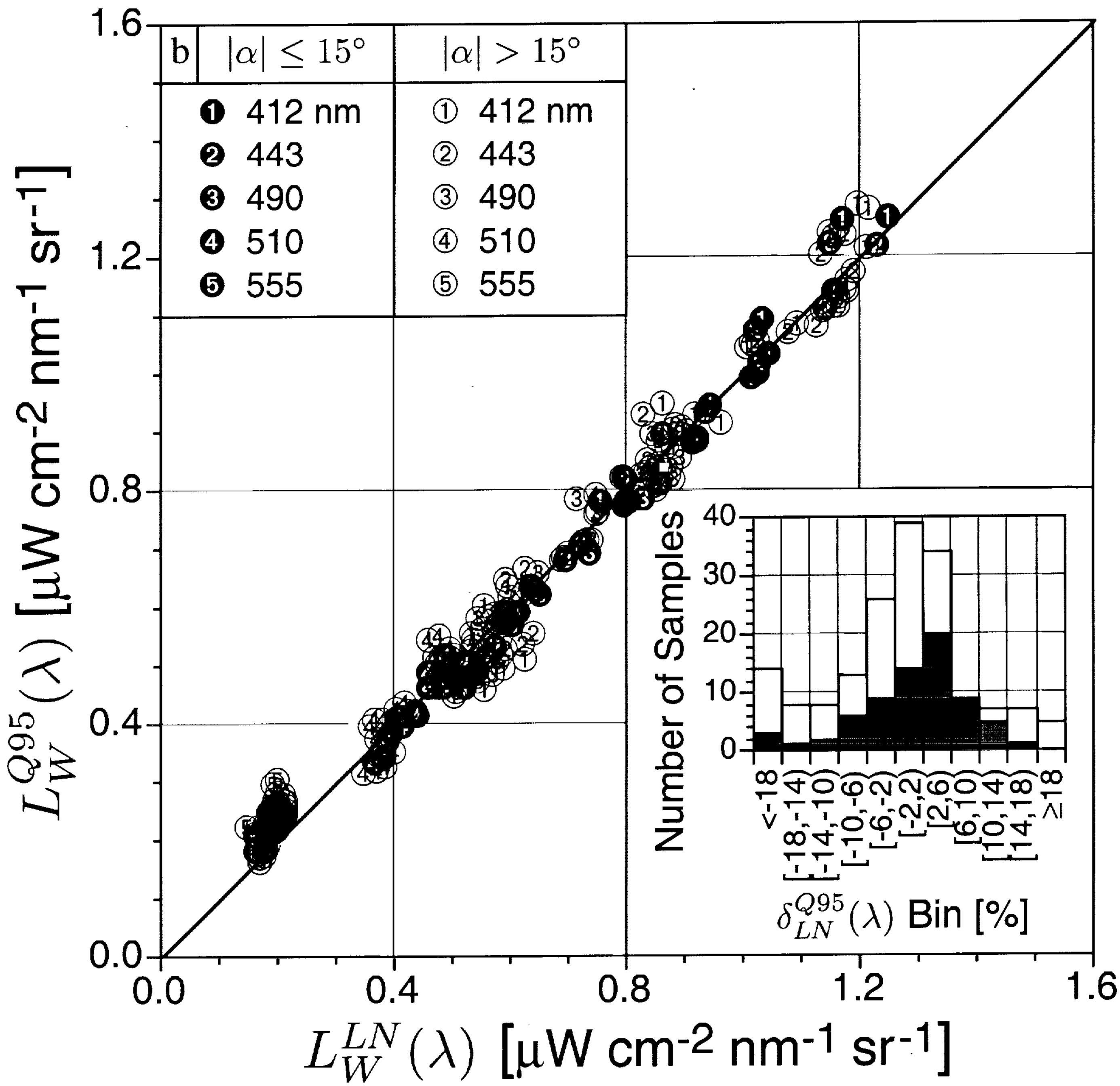
b
$|\alpha| \leq 15°$
$|\alpha| > 15°$
❶ 412 nm
❷ 443
❸ 490
❹ 510
❺ 555
① 412 nm
② 443
③ 490
④ 510
⑤ 555
1.6
1.2
0.8
0.4
0.0
$L_W^{Q95}(\lambda)$ [μW cm-2 nm-1 sr-1]
$L_W^{LN}(\lambda)$ [μW cm-2 nm-1 sr-1]
Number of Samples
40
30
20
10
0
<-18
[-18,-14)
[-14,-10)
[-10,-6)
[-6,-2)
[-2,2)
[2,6)
[6,10)
[10,14)
[14,18)
≥18
$\delta_{LN}^{Q95}(\lambda)$ Bin [%]

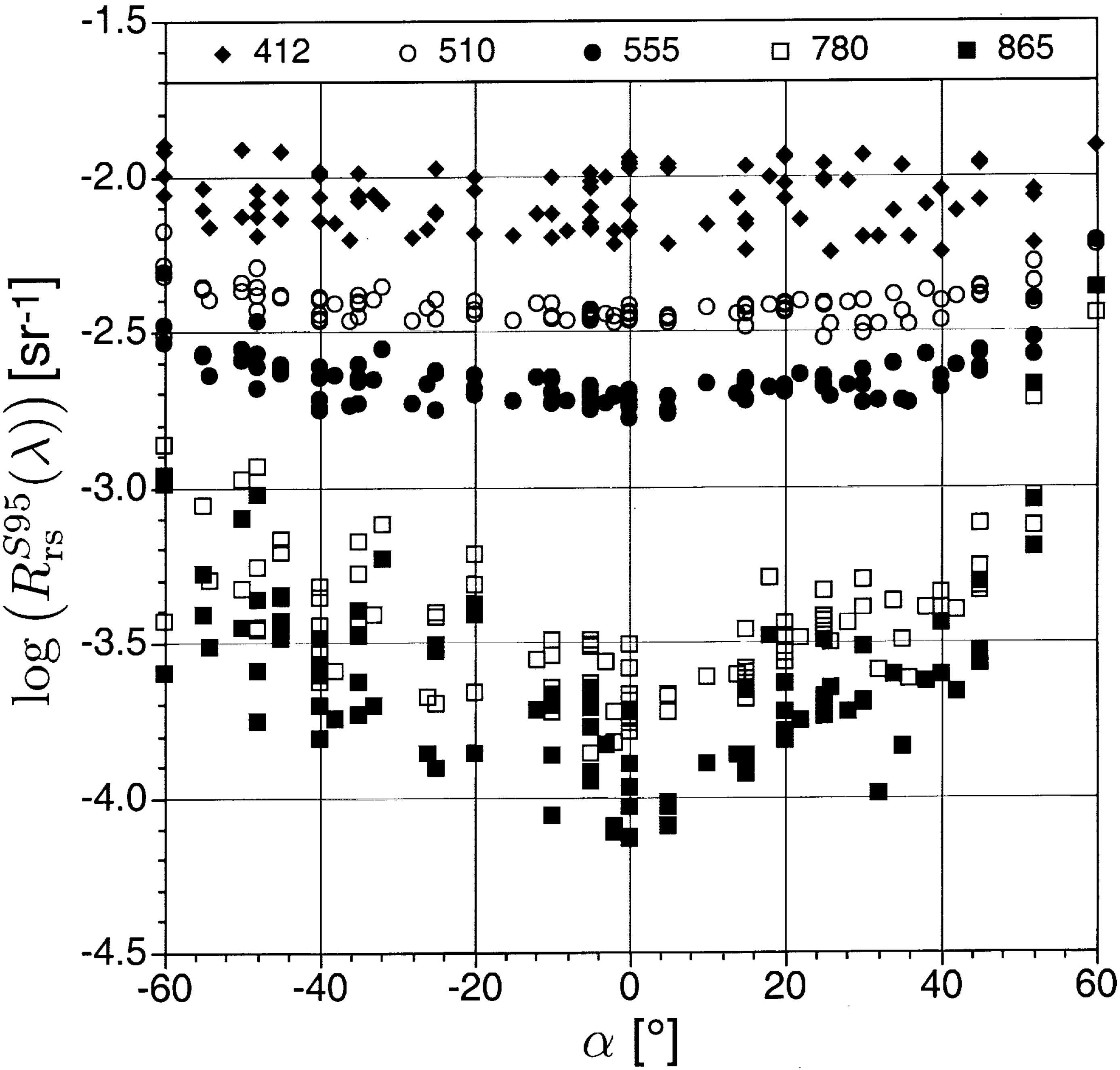
412
510
555
780
865
-1.5
-2.0
-2.5
-3.0
-3.5
-4.0
-4.5
-60
-40
-20
0
20
40
60
$\log\left(R_{\mathrm{rs}}^{S95}(\lambda)\right)$ [sr-1]
α [°]

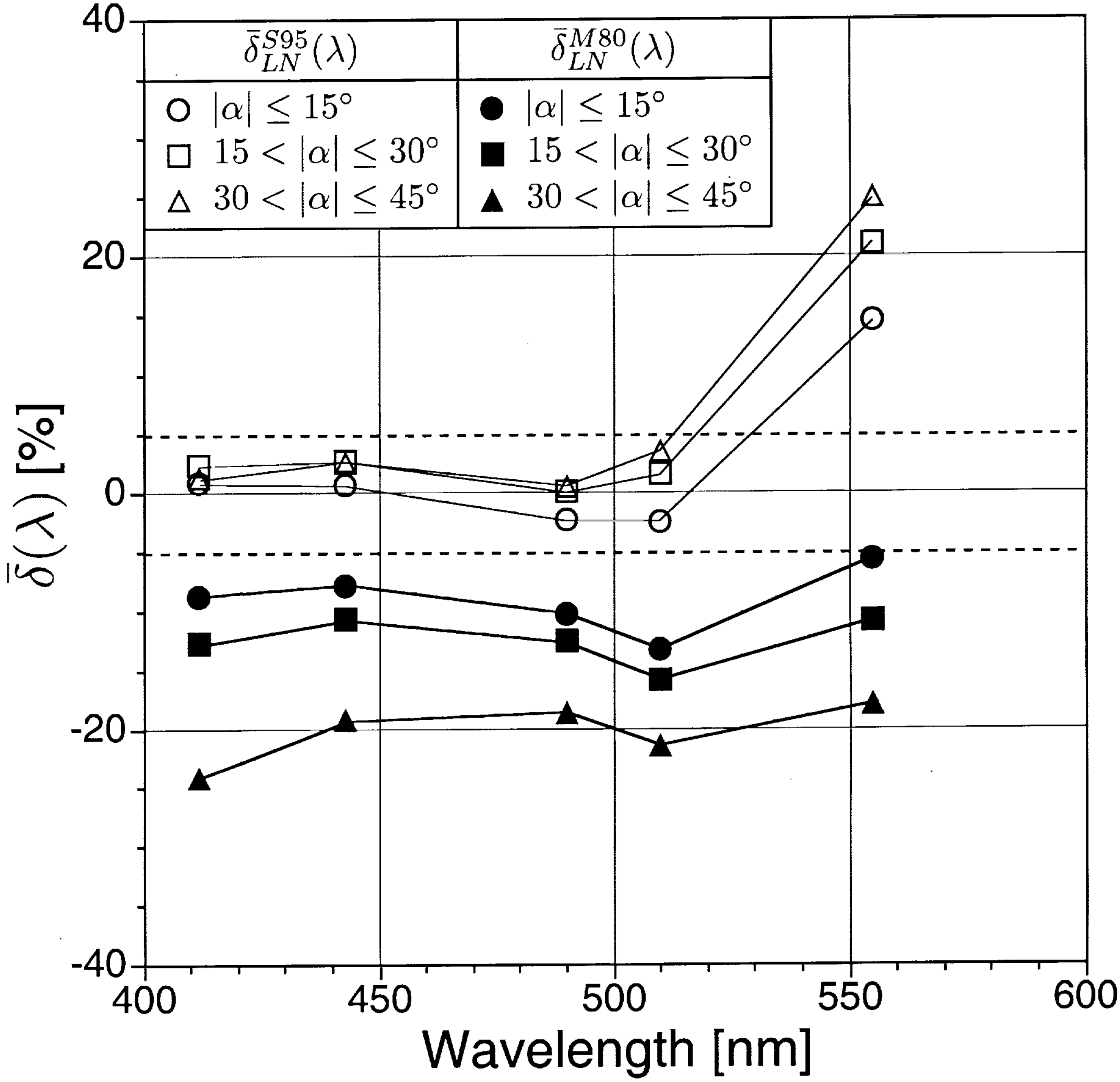

$\bar{\delta}_{LN}^{S95}(\lambda)$
$|\alpha| \leq 15°$
$15 < |\alpha| \leq 30°$
$30 < |\alpha| \leq 45°$
$\bar{\delta}_{LN}^{M80}(\lambda)$
$|\alpha| \leq 15°$
$15 < |\alpha| \leq 30°$
$30 < |\alpha| \leq 45°$
40
20
0
-20
-40
400
450
500
550
600
Wavelength [nm]
$\bar{\delta}(\lambda)$ [%]